Copyright note

Pål Næverlid Sævik (first author) Bergen, 09.12.2014

Transport in Porous Media manuscript No.
(will be inserted by the editor)

A 3D computational study of effective medium methods applied to fractured media

Pål Næverlid Sævik · Inga Berre · Morten Jakobsen · Martha Lien

Received: date / Accepted: date

Abstract This work evaluates and improves upon existing effective medium methods for permeability upscaling in fractured media. Specifically, we are concerned with the asymmetric self-consistent, symmetric self-consistent and differential methods. In effective medium theory, inhomogeneity is modeled as ellipsoidal inclusions embedded in the rock matrix. Fractured media correspond to the limiting case of flat ellipsoids, for which we derive a novel set of simplified formulas. The new formulas have improved numerical stability properties, and require a smaller number of input parameters. To assess their accuracy, we compare the analytical permeability predictions with accurate, three-dimensional finite-element simulations. We also compare the results with a semi-analytical method based on percolation theory and curve fitting, which represents an alternative upscaling approach. A large number of cases is considered, with varying fracture aperture, density, matrix/fracture permeability contrast, orientation, shape and number of fracture sets. The differential method is seen to be the best choice for sealed fractures and thin open fractures. For high-permeable, connected fractures, the semi-analytical method provide the best fit to the numerical data, whereas the differential method breaks down. The two self-consistent methods can be used for both unconnected and connected fractures, although the asymmetric method is somewhat unreliable for sealed fractures. For open fractures, the symmetric method is generally the more accurate for moderate fracture densities, but only the asymmetric method is seen to have correct asymptotic behaviour. The asymmetric method is also surprisingly accurate at predicting percolation thresholds.

Keywords homogenization, fractures, effective permeability, numerical upscaling, 3D, effective medium theory

P. N. Sævik (✉) · I. Berre
Department of Mathematics, University of Bergen, P.O. Box 7800, 5007 Bergen, Norway
E-mail: pal.saevik@math.uib.no

M. Lien
Uni Research, Centre for Integrated Petroleum Research, P.O. Box 7800, 5007 Bergen, Norway

M. Jakobsen
Department of Earth Science, University of Bergen, P.O. Box 7800, 5007 Bergen, Norway

1 Introduction

Fluid flow in fractured rocks is of great importance in many industrial and environmental applications, such as hydrology, petroleum engineering, nuclear waste disposal, geothermal energy and subsurface CO_2 storage. The presence of fractures can increase the permeability by several orders of magnitude, and create large anisotropy effects in the medium. Geological formations may also contain planar discontinuities that obstruct fluid flow, such as deformation bands (Fossen et al, 2007). In this paper, a *fracture* is defined as any kind of planar feature representing a permeability discontinuity. We consider both permeability-enhancing and permeability-reducing fractures, which are referred to as *open* and *sealed*, respectively.

Fractures occur in geological formations at different scales. Large structures, such as major faults, are usually visible on seismic data and can be accounted for explicitly in the geological model. In this work, we are concerned with fractures on a smaller scale which are characterized by statistical parameters. The presence of small-scale fractures (sometimes called *diffuse fractures*) can often be inferred from the rock type, the stress history of the rock, and surrounding geological structures. For instance, small fractures with specific primary orientations are expected to be present in the vicinity of faults and folds (Singhal and Gupta, 1999). In addition, borehole data may provide specific information on the average aperture, size and spacing of the fractures.

From a macroscopic perspective, a rock containing large numbers of evenly distributed fractures will behave as a homogeneous material with respect to properties like single-phase permeability, thermal conductivity and electrical conductivity. These properties are mathematically analogous, due to the similarity between their respective constitutive relations. Although we focus on fluid permeability in this work, the methods we describe can be applied to all the aforementioned physical properties. This feature makes the methods attractive for joint inversion applications (Jakobsen et al, 2007).

Homogenization, or upscaling, is the process of finding the effective physical properties of a heterogeneous rock/fracture system. A straightforward approach is numerical upscaling, in which a model of the fracture geometry is generated and meshed. Thereafter, a standard numerical simulation algorithm (such as the finite element or finite volume method) is used to calculate the average flux through the medium, from which the effective permeability is found. Since the method is computationally expensive, numerical upscaling is usually performed with a coarse mesh and simplified geometry, adding a significant uncertainty to the permeability estimate.

An alternative is to use analytical homogenization methods to estimate the effective permeability. In this paper, we are concerned with effective medium theory, which has been suggested as a promising upscaling technique for fractured media (Fokker, 2001; Pozdniakov and Tsang, 2004; Barthélémy, 2008; Berryman and Hoversten, 2013). The most popular variants of effective medium methods used in the literature are the asymmetric self-consistent method, the symmetric self-consistent method and the differential method. In all of these, fractures are represented as ellipsoidal-shaped inclusions within an otherwise homogeneous matrix. Originally due to Bruggeman (1935), effective medium approximations are known to be accurate for near-homogeneous materials containing only a few non-intersecting inclusions (Torquato, 2002). Strongly fractured media, on the other hand, are characterized by a large number of intersecting, flat inclusions of very high or very low intrinsic permeability. To determine if the methods can be used for this type of geometry, comparisons with accurate numerical experiments are needed.

Some numerical tests of effective medium theory have been conducted, with encouraging results (Zimmerman and Yeo, 2000; Pozdniakov and Tsang, 2004; Barthélémy, 2008; Tawerghi and Yi, 2009). These works are limited to spherical/near-spherical inclusions, or isotropic/transversely isotropic media, or two-dimensional geometries. To our knowledge, a systematic evaluation of effective medium theory for three-dimensional, fully anisotropic fractured media has not yet been performed. The present work seeks to fill this gap by comparing effective medium predictions with accurate numerical simulations. Similar studies have already been performed for a different class of analytical upscaling methods Bogdanov et al (2007); Mourzenko et al (2011), whose predictions are included in this paper for comparison.

In order to present a complete and unified description of the assessed methods, Section 2 of this paper contains an overview of effective medium theory and its variants. The theory is based on the analytical solution of the single-ellipsoid inclusion problem (Section 2.1) and the dilute limit approximation (Section 2.2). These relations are used to derive the asymmetric self-consistent method (Section 2.3), the symmetric self-consistent method (Section 2.4) and the differential method (Section 2.5).

In Section 3, we develop a novel set of formulas in the limiting case where the inclusion thickness is much less than the inclusion radius (i.e., flat inclusions). This is precisely the case of interest when considering fractured media, since the aperture of a fracture by definition is much smaller than its lateral extent. The new formulas have improved numerical stability properties, and require fewer parameters than the original formulations.

In Section 4, we briefly discuss the semi-analytical upscaling method of Mourzenko et al (2011), which is based on curve-fitting and percolation theory. The method is is applicable when either the matrix permeability is neglible, or when the fracture density is large, and is included for comparison with the effective medium methods.

The numerical results are presented in Section 5. First, details on the computational procedure are outlined, and technical difficulties regarding meshing are addressed (Section 5.1), as well as numerical convergence issues (Section 5.2). The results for open and sealed fractures are discussed in Section 5.3 and 5.4, respectively. To identify the range of applicability of the methods, a large number of cases is considered, with varying fracture aperture, matrix/fracture permeability contrast, fracture density, orientation, shape and number of fracture sets.

2 Review of effective medium theory

In effective medium theory, fractures are modeled as thin, ellipsoidal inclusions, scattered randomly within a matrix of homogeneous permeability. It is commonly assumed that all the fractures are spheroidal, so that the radius r and aspect ratio ω is sufficient to describe their size and shape. In this work, we allow the eccentricity η to vary, to cover a wider specter of applications. An overview of additional parameters for characterizing ellipsoidal fractures, and their relation to each other, is given in Tab. 1. For simplicity, we assume that the fractures can be divided into N distinct sets, according to their shape, size, orientation and permeability. Each fracture set, as well as the rock matrix, is referred to as a separate material phase, and we use subscripts to denote which phase is associated with a certain property. The theory is easily extended to continuous distributions of fracture parameters, by replacing fracture set summations with integrals when appropriate.

Symbol	Description
$\mathcal{N}$	Number of fractures per volume
l_1, l_2, l_3	Length of semi-axes, decreasing order
$\mathbf{e}_1, \mathbf{e}_2, \mathbf{e}_3$	Direction of semi-axes
$\mathbf{H} = \sum l_k^2/l_1^2 \mathbf{e}_k \mathbf{e}_k$	Fracture shape and orientation (tensor)
$r = l_1$	Length of largest semi-axis
$\eta = l_2/l_1$	Eccentricity
$\omega = l_3/l_1$	Thickness ratio
$\varepsilon = \mathcal{N} r^3$	Fracture density
$a = \frac{4}{3}\omega r$	Mean fracture aperture
$\phi = \frac{4}{3}\pi\varepsilon\eta\omega$	Porosity (volume fraction)
$S = \pi\mathcal{N} r^2\eta$	Fracture surface per volume
$s = 1/\pi\mathcal{N} r^2\eta$	Fracture spacing
$K = a^2/12$	Permeability of open fracture
$\cos\beta = \mathbf{e}_3 \cdot \mathbf{Z}$	Dip angle ($\mathbf{Z}$ is a unit vector pointing upwards)
$\cos\alpha = \csc\beta\, \mathbf{e}_3 \cdot \mathbf{N}$	Dip direction ($\mathbf{N}$ is a unit vector pointing north)

Tab. 1: Parameters for characterizing ellipsoidal fractures

Effective medium theory requires that the fractures are regarded as Darcy media, i.e., the average flow velocity within a fracture is assumed to be linearly dependent on the pressure gradient. For a fracture with aperture a, a simple estimate for the tangential permeability is given by $K_t = a^2/12$. This relation, known as the *cubic law*, is derived by assuming Darcy flow in the rock matrix and Stokes flow inside the fracture. More accurate approximations can be found by accounting for fracture wall roughness (Zimmerman and Yeo, 2000) and viscous forces at the fracture-matrix interface (Vernerey, 2012). In the normal direction, the fluid experiences no flow resistance within the fracture. The equivalent permeability in the normal direction is therefore larger than the tangential component, but in this paper we set them to be equal. Earlier work by Barthélémy (2008) shows that this simplification has no effect on the upscaled rock permeability.

2.1 The single-inclusion problem

Effective medium methods depend on the solution of an auxiliary problem that involves only a single matrix inclusion. The problem can be formulated as finding the average pressure gradient $\mathbf{J}_i$ within a single ellipsoidal inclusion of family i with intrinsic permeability $\mathbf{K}_i$, embedded in a matrix of homogeneous permeability $\mathbf{M}$, subject to an externally applied pressure gradient $\mathbf{J}_{far}$. By solving the Laplace equation in spherical coordinates (Eshelby, 1957; Landau and Lifshitz, 1960), the solution to the single-inclusion problem is found to be

$$\mathbf{J}_i = \mathbf{R}_i(\mathbf{M})\,\mathbf{J}_{far}, \tag{1}$$

$$\mathbf{R}_i(\mathbf{M}) = \left(\mathbf{I} + \mathbf{M}^{-\frac{1}{2}}\mathbf{A}_i\mathbf{M}^{-\frac{1}{2}}(\mathbf{K}_i - \mathbf{M})\right)^{-1}, \tag{2}$$

where $\mathbf{R}_i$ is the *field concentration tensor*, $\mathbf{A}_i$ is the *depolarization tensor* and $\mathbf{M}^{\frac{1}{2}}$ is the positive definite square root of $\mathbf{M}$. $\mathbf{A}_i$ is a nonlinear function of the permeability, shape and orientation of the inclusion, which are all properties of the inclusion family i.

If the background permeability $\mathbf{M}$ is isotropic, the expression for $\mathbf{A}_i$ is found in many sources (see, for instance, Eshelby (1957); Landau and Lifshitz (1960); Torquato (2002)). In effective medium theory, $\mathbf{M}$ is substituted with the effective permeability of the medium, which may be anisotropic even though the intrinsic permeability of the matrix is isotropic. Thus, we require the solution of the single-inclusion problem with an anisotropic background permeability, which is slightly more complicated. Here, we only describe the resulting formula, and refer to Barthélémy (2008) for a complete derivation. To avoid cluttering the formulas, we ignore the inclusion family subscript i for the remainder of this section.

First, let us introduce the *shape tensor*, which describes the shape of the ellipsoidal inclusion. In dyadic notation, the tensor is written as

$$\mathbf{H} = \sum_{k=1}^{3} h_k \mathbf{e}_k \mathbf{e}_k^\top, \tag{3}$$

where $\mathbf{e}_1, \mathbf{e}_2, \mathbf{e}_3$ are unit vectors directed along the axes of the ellipsoid and $1 = h_1 \geq \eta^2 = h_2 \geq \omega^2 = h_3$ are the squared semi-axis lengths, scaled by the square of the largest axis. The tensor has the property that

$$\mathbf{x}^\top \mathbf{H}^{-1} \mathbf{x} \leq 1 \tag{4}$$

defines an ellipsoid with the same shape and orientation as the inclusion. We further define a *transformed ellipsoid*, given by the tensor

$$\tilde{\mathbf{H}} = \sqrt[3]{\det \mathbf{M}}\, \mathbf{M}^{-\frac{1}{2}} \mathbf{H} \mathbf{M}^{-\frac{1}{2}}. \tag{5}$$

Observe that the ellipsoids defined by $\mathbf{H}$ and $\tilde{\mathbf{H}}$ have the same volume, since $\det \tilde{\mathbf{H}} = \det \mathbf{H} = \eta^2 \omega^2$. The two shape tensors are equal if the background permeability $\mathbf{M}$ is isotropic.

The next step is to diagonalize $\tilde{\mathbf{H}}$ using an eigenvalue decomposition,

$$\tilde{\mathbf{H}} = \sum_{k=1}^{3} \tilde{h}_k \tilde{\mathbf{e}}_k \tilde{\mathbf{e}}_k^\top. \tag{6}$$

We assume that the eigenvalues $\tilde{h}_1, \tilde{h}_2, \tilde{h}_3$, which are the squared semi-axes of the transformed ellipsoid, are ordered such that $\tilde{h}_1 \geq \tilde{h}_2 \geq \tilde{h}_3$. Finally, the depolarization tensor is given by

$$\mathbf{A} = \eta\, \omega \sum_{k=1}^{3} \Lambda_k \tilde{\mathbf{e}}_k \tilde{\mathbf{e}}_k^\top, \tag{7}$$

where

$$\Lambda_k = \frac{1}{2} \int_0^\infty \frac{dt}{\left(t + \tilde{h}_k\right) \sqrt{\left(t + \tilde{h}_1\right)\left(t + \tilde{h}_2\right)\left(t + \tilde{h}_3\right)}}. \tag{8}$$

If $\mathbf{M}$ is isotropic, there are some special cases in which the above elliptic integral can be evaluated analytically (Carlson and Gustafson, 1993). In general, however, the integral has to be solved numerically. It is common to express (8) using Legendre elliptic integrals, but

a direct evaluation using duplication (Carlson, 1995) or half- and double-argument transformations (Fukushima, 2011a) is preferred to avoid cancellation errors in the commonly occurring situation where $\tilde{h}_1 \approx \tilde{h}_2$. Fast and efficient implementations of these algorithms are widely available. Furthermore, it can be shown that the sum of the eigenvalues of $\mathbf{A}$ is equal to 1 (Eshelby, 1957). Thus, if the first elliptic integrals Λ_1 and Λ_2 are found, the third is easily calculated as

$$\Lambda_3 = \frac{1}{\eta\omega} - \Lambda_1 - \Lambda_2. \tag{9}$$

In the limiting case where one of the ellipsoid axes approaches zero, Λ_1 and Λ_2 reduce to *complete* elliptic integrals, which are efficiently evaluated using a series expansion (Fukushima, 2011b). This case is of particular interest for fractured media, since fractures are modeled as flat ellipsoids. In Section 3, we further investigate how the expression for $\mathbf{R}_i$ should be formulated when i is a family of flat inclusions.

2.2 Dilute limit approximation

To show how the single-inclusion problem is used to derive permeability approximations, we start by considering a dilute dispersion of ellipsoidal inclusions within a homogeneous matrix. On the macroscopic scale, the composite behaves as a homogeneous material with permeability $\mathbf{K}_e$, according to the definition

$$\mathbf{K}_e\mathbf{J}_e = \sum_{i=0}^{N} \phi_i \mathbf{K}_i \mathbf{J}_i, \tag{10}$$

$$\mathbf{J}_e = \sum_{i=0}^{N} \phi_i \mathbf{J}_i, \tag{11}$$

where N is the number of inclusion families, and ϕ_i, $\mathbf{K}_i$ and $\mathbf{J}_i$ are the volume fraction, permeability and average pressure gradient of phase i, respectively. By convention, we let the subscript 0 denote the matrix phase. Since the inclusions are well-separated, the pressure gradient within each of them can be approximated by the solution of the single-inclusion problem. Setting $\mathbf{J}_{far} = \mathbf{J}_e$ and $\mathbf{M} = \mathbf{K}_0$ in (1), we have the expression

$$\mathbf{J}_i = \mathbf{R}_i(\mathbf{K}_0)\,\mathbf{J}_e, \quad i \neq 0. \tag{12}$$

We insert (12) into (10), and use (11) to eliminate $\mathbf{J}_0$, arriving at

$$\mathbf{K}_e = \mathbf{K}_0 + \sum_{i=1}^{N} \phi_i (\mathbf{K}_i - \mathbf{K}_0)\,\mathbf{R}_i(\mathbf{K}_0). \tag{13}$$

This is the *dilute limit approximation* for the effective permeability, which is valid only when the number of inclusions per volume is small (Torquato, 2002).

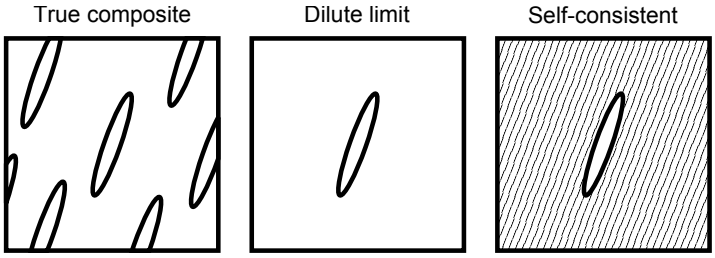

Fig. 1: The self-consistent assumption

2.3 The asymmetric self-consistent method

In equation (13), we assumed that the pressure gradient within each inclusion is unaffected by neighboring inclusions. One way of compensating for this, is to substitute $\mathbf{K}_0$ in (12) with $\mathbf{K}_e$ (Pozdniakov and Tsang, 2004),

$$\mathbf{J}_i = \mathbf{R}_i\left(\mathbf{K}_e\right)\mathbf{J}_e, \quad i \neq 0. \tag{14}$$

In other words, we approximate the hydraulic response by assuming that the neighborhood of each inclusion is a homogeneous material with permeability $\mathbf{K}_e$ (see Fig. 1). Combining again with (10) and (11), we have

$$\mathbf{K}_e = \mathbf{K}_0 + \sum_{i=1}^{N} \phi_i \left(\mathbf{K}_i - \mathbf{K}_0\right)\mathbf{R}_i\left(\mathbf{K}_e\right). \tag{15}$$

This is the *asymmetric self-consistent approximation*, also known as the *average field approximation* (Milton, 2002). Since (15) defines $\mathbf{K}_e$ implicitly, one must use numerical techniques to calculate the effective permeability. The simple fixed point iteration scheme

$$\mathbf{K}_{e,n+1} = \mathbf{K}_0 + \sum_{i=1}^{N} \phi_i \left(\mathbf{K}_i - \mathbf{K}_0\right)\mathbf{R}_i\left(\mathbf{K}_{e,n}\right) \tag{16}$$

seems to converge reasonably fast if $\|\mathbf{K}_e\| \geq \|\mathbf{K}_0\|$. When $\|\mathbf{K}_e\| \leq \|\mathbf{K}_0\|$, our experience is that the modified scheme

$$\mathbf{K}_{e,n+1}^{-1} = \mathbf{K}_0^{-1} + \sum_{i=1}^{N} \phi_i \mathbf{K}_0^{-1}\left(\mathbf{K}_0 - \mathbf{K}_i\right)\mathbf{R}_i\left(\mathbf{K}_{e,n}\right)\mathbf{K}_{e,n}^{-1} \tag{17}$$

has better convergence properties.

2.4 The symmetric self-consistent method

A possible drawback of (15) is that its permeability estimates may not be *physically realizable* (Milton, 2002). That is, given the input data (inclusion shapes, orientations, permeabilities and volume fractions), it may not exist a consistent microstructural configuration such that the permeability estimate is attained. We can obtain a realizable self-consistent

scheme by treating both the matrix and the fractures as ellipsoidal inclusions (Torquato, 2002; Barthélémy, 2008). In other words, we set

$$\mathbf{J}_i = \mathbf{R}_i\left(\mathbf{K}_e\right)\mathbf{J}_{far}, \quad i \in \{0, 1, \ldots, N\}, \tag{18}$$

and calculate $\mathbf{R}_i\left(\mathbf{K}_e\right)$ using (2) for all i, including the matrix phase. To calculate $\mathbf{R}_0$, we must construct an ellipsoidal shape (with shape tensor $\mathbf{H}_0$) that somehow resemble the geometry of the space between the inclusions. For fractured media, Barthélémy (2008) suggested using a weighted average of the inclusion shape tensors $\{\mathbf{H}_1, \ldots, \mathbf{H}_N\}$, but the given expression is ill-conditioned if there are less than three non-parallel fracture sets. Since it is not obvious how to choose an optimal value for $\mathbf{H}_0$, we have simply set $\mathbf{H}_0 = \mathbf{I}$ in the present work.

The permeability is found by inserting (18) into (10), and using (11) to eliminate $\mathbf{J}_e$,

$$\mathbf{K}_e \sum_{i=0}^{N} \phi_i \mathbf{R}_i\left(\mathbf{K}_e\right) = \sum_{i=0}^{N} \phi_i \mathbf{K}_i \mathbf{R}_i\left(\mathbf{K}_e\right). \tag{19}$$

This relation is called the *symmetric self-consistent approximation*, also known as the *coherent potential approximation*. By rearranging, we obtain

$$\mathbf{K}_e = \mathbf{K}_0 + \sum_{i=1}^{N} \frac{\phi_i}{\phi_0}\left(\mathbf{K}_i - \mathbf{K}_e\right)\mathbf{R}_i\left(\mathbf{K}_e\right)\mathbf{R}_0^{-1}\left(\mathbf{K}_e\right), \tag{20}$$

which can be evaluated using the same numerical techniques as for (15).

In the literature, the distinction between the symmetric and asymmetric self-consistent methods is not always made clear. Usually, only one of them are used, while the other is not mentioned. For instance, the method used by Fokker (2001); Torquato (2002); Barthélémy (2008) is the symmetric one, while Pozdniakov and Tsang (2004) use the asymmetric method. Two literature references that mentions both methods are Willis (1977) and Milton (2002).

It is well-known that both self-consistent methods described in this paper may predict a sudden permeability increase when the inclusion volume fractions reach a critical level, if the contrast between the inclusion and matrix permeabilities is large. Within the context of fracture upscaling, it has been suggested that this behaviour can be identified with *percolation*, which is the transition from unconnected to connected fracture networks (Pozdniakov and Tsang, 2004; Barthélémy, 2008; Pouya and Ghabezloo, 2010). Unfortunately, there is no theoretical result justifying this conjecture, and many authors regard the self-consistent percolation estimates as spurious(Guéguen et al, 1997; Torquato, 2002). Numerical simulations are therefore valuable in order to assess the feasibility of the methods in this regime.

2.5 The differential method

Another popular effective medium technique, which is also physically realizable, is the *differential effective medium method*. To derive the method, let A be a material composed of ellipsoids, embedded in a host matrix. Let material B be identical to A, except that a few more inclusions have been added. To preserve the ratio between the inclusion families, we require that

$$\frac{\phi_i^{\mathrm{A}}}{1-\phi_0^{\mathrm{A}}} = \frac{\phi_i^{\mathrm{B}}}{1-\phi_0^{\mathrm{B}}} \tag{21}$$

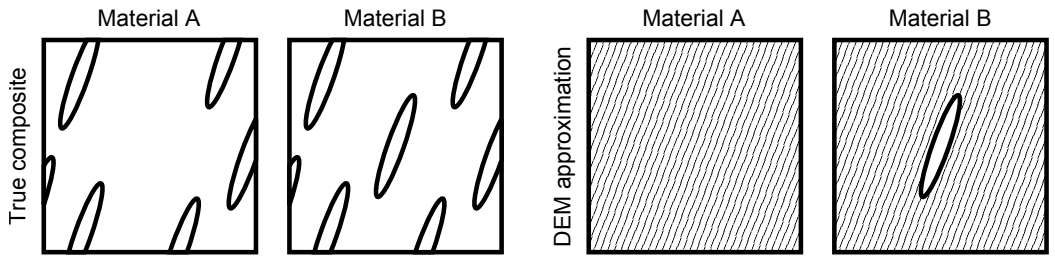

Fig. 2: The differential effective medium approximation

for all $i \neq 0$, where the superscripts denote the material. There are other variants of the differential method where the ratio is not preserved, but these are not considered here (Norris et al, 1985).

We approximate $\mathbf{K}_e^{\mathrm{B}}$ by assuming that all of B, except for the extra inclusions, behaves like a homogeneous material with permeability $\mathbf{K}_e^{\mathrm{A}}$ (see Fig. 2). With this assumption, we can use the dilute limit approximation (13) to obtain

$$\mathbf{K}_e^{\mathrm{B}} = \mathbf{K}_e^{\mathrm{A}} + \sum_{i=1}^{N} \Delta\phi_i \left(\mathbf{K}_i - \mathbf{K}_e^{\mathrm{A}}\right) \mathbf{R}_i \left(\mathbf{K}_e^{\mathrm{A}}\right), \tag{22}$$

where

$$\Delta\phi_i = \phi_i^{\mathrm{B}} - \phi_i^{\mathrm{A}}. \tag{23}$$

We can rewrite this expression using (21) and some algebraic manipulation,

$$\phi_i^{\mathrm{B}} - \phi_i^{\mathrm{A}} = \left(1 - \phi_0^{\mathrm{B}}\right) \frac{\phi_i^{\mathrm{B}} - \phi_i^{\mathrm{A}}}{1 - \phi_0^{\mathrm{B}}} \tag{24}$$

$$= \left(1 - \phi_0^{\mathrm{B}}\right) \left(\frac{\phi_i^{\mathrm{A}}}{1 - \phi_0^{\mathrm{A}}} - \frac{\phi_i^{\mathrm{A}}}{1 - \phi_0^{\mathrm{B}}} \right) \tag{25}$$

$$= \frac{\phi_i^{\mathrm{A}}}{1 - \phi_0^{\mathrm{A}}} \left(\phi_0^{\mathrm{A}} - \phi_0^{\mathrm{B}}\right). \tag{26}$$

Inserting into (22) and rearranging, we get

$$\frac{\mathbf{K}_e^{\mathrm{B}} - \mathbf{K}_e^{\mathrm{A}}}{\phi_0^{\mathrm{B}} - \phi_0^{\mathrm{A}}} = -\sum_{i=1}^{N} \frac{\phi_i^{\mathrm{A}}}{1 - \phi_0^{\mathrm{A}}} \left(\mathbf{K}_i - \mathbf{K}_e^{\mathrm{A}}\right) \mathbf{R}_i \left(\mathbf{K}_e^{\mathrm{A}}\right). \tag{27}$$

In the limit as $\Delta\phi_0 \to 0$, we obtain the differential equation

$$\frac{d\mathbf{K}_e}{d\phi_0} = -\sum_{i=1}^{N} \frac{\phi_i}{1 - \phi_0} \left(\mathbf{K}_i - \mathbf{K}_e\right) \mathbf{R}_i \left(\mathbf{K}_e\right). \tag{28}$$

To obtain a permeability estimate from (28), an initial value for $\mathbf{K}_e$ is required. A natural choice is to set $\mathbf{K}_e = \mathbf{K}_0$ at $\phi_0 = 1$, both because the permeability is known exactly at this point, and because the method is based on the dilute limit approximation (13) which is more accurate when ϕ_0 is close to 1. In general, it is not possible to integrate (28) analytically, but the equation can be solved numerically using a standard explicit Runge-Kutta or multistep method.

3 Effective medium approximations for flat inclusions

In the previous derivation of the effective medium methods, we have used volume fractions to describe the amount of inclusions present in the matrix. This is the standard parameter choice when effective medium methods are discussed in the literature. However, fractures normally occupy a very small part of the overall volume, and it may be more appropriate to describe the fracture amount by another measure. Several different measures of fracture density are used in the literature, like fracture surface area per volume, or fracture spacing. We have chosen to use the following dimensionless definition of fracture density,

$$\varepsilon_i = \mathscr{N}_i r_i^3, \tag{29}$$

where $\mathscr{N}_i$ is the number per volume of inclusions belonging to phase i, and r_i is the length of the largest inclusion semi-axis.

In the following, we derive a novel set of effective-medium formulas in the limiting case where the ratio ω_i of the shortest to the longest semi-axis approaches zero. Although $\omega_i > 0$ in practice, the ratio is usually so small that the differences between the exact and limiting expressions are negligible.

The effective medium methods derived in Section 2 are the asymmetric self-consistent method (15), the symmetric self-consistent method (20) and the differential method (28). Using definition (29), these expressions become

$$\mathbf{K}_e = \mathbf{K}_0 + \sum_{i=1}^{N} \frac{\varepsilon_i}{\phi_0} \mathbf{K}_e \left(\mathbf{R}_i^{\mathrm{B}} - \mathbf{R}_i^{\mathrm{C}} \right) \mathbf{R}_0^{-1}, \qquad \text{(Symmetric self-consistent)} \tag{30}$$

$$\mathbf{K}_e = \mathbf{K}_0 + \sum_{i=1}^{N} \varepsilon_i \left(\mathbf{K}_e \mathbf{R}_i^{\mathrm{B}} - \mathbf{K}_0 \mathbf{R}_i^{\mathrm{C}} \right), \qquad \text{(Asymmetric self-consistent)} \tag{31}$$

$$\frac{d\mathbf{K}_e}{d\varepsilon_{sum}} = \sum_{i=1}^{N} \frac{\varepsilon_i}{\varepsilon_{sum}} \mathbf{K}_e \left(\mathbf{R}_i^{\mathrm{B}} - \mathbf{R}_i^{\mathrm{C}} \right), \qquad \text{(Differential method)} \tag{32}$$

where

$$\mathbf{R}_i^{\mathrm{B}} = \frac{4}{3} \pi \eta_i \omega_i \mathbf{K}_e^{-1} \mathbf{K}_i \mathbf{R}_i, \tag{33}$$

$$\mathbf{R}_i^{\mathrm{C}} = \frac{4}{3} \pi \eta_i \omega_i \mathbf{R}_i, \tag{34}$$

$$\varepsilon_{sum} = \sum_{i=1}^{N} \varepsilon_i. \tag{35}$$

The tensors $\mathbf{R}_0, \ldots, \mathbf{R}_N$ are all evaluated using $\mathbf{K}_e$ as the background medium. Alternatively, Equations (30)-(32) can be expressed using inverse permeabilities,

$$\mathbf{K}_e^{-1} = \mathbf{K}_0^{-1} + \sum_{i=1}^{N} \frac{\varepsilon_i}{\phi_0} \left(\mathbf{R}_i^{\mathrm{C}} - \mathbf{R}_i^{\mathrm{B}} \right) \mathbf{R}_0^{-1} \mathbf{K}_0^{-1}, \qquad \text{(Symmetric self-consistent)} \tag{36}$$

$$\mathbf{K}_e^{-1} = \mathbf{K}_0^{-1} + \sum_{i=1}^{N} \varepsilon_i \left(\mathbf{R}_i^{\mathrm{C}} - \mathbf{K}_0^{-1} \mathbf{K}_e \mathbf{R}_i^{\mathrm{B}} \right) \mathbf{K}_e^{-1}, \qquad \text{(Asymmetric self-consistent)} \tag{37}$$

$$\frac{d\mathbf{K}_e^{-1}}{d\varepsilon_{sum}} = \sum_{i=1}^{N} \frac{\varepsilon_i}{\varepsilon_{sum}} \left(\mathbf{R}_i^{\mathrm{C}} - \mathbf{R}_i^{\mathrm{B}} \right) \mathbf{K}_e^{-1}, \qquad \text{(Differential method)} \tag{38}$$

which is often more appropriate when sealed fractures dominate the system. Note that the role of $\mathbf{R}_i^{\mathrm{B}}$ and $\mathbf{R}_i^{\mathrm{C}}$ is very different for open and sealed fractures. If the fractures are open ($\mathbf{K}_i \gg \mathbf{K}_e$), $\mathbf{R}_i^{\mathrm{B}}$ is much larger than $\mathbf{R}_i^{\mathrm{C}}$, and the latter can be set to zero since it does not contribute significantly to the computed effective permeability. For sealed fractures, we have the opposite situation, as $\mathbf{R}_i^{\mathrm{C}}$ is much larger than $\mathbf{R}_i^{\mathrm{B}}$ in this case.

We now introduce alternative expressions for $\mathbf{R}_i^{\mathrm{B}}$ and $\mathbf{R}_i^{\mathrm{C}}$ that are suitable for studying the behavior of effective medium methods for small values of ω_i. To avoid cluttering the formulas, we ignore the fracture family subscript i in the remainder of the section. By inserting (2) into (33), (34) and rearranging, we get

$$\mathbf{R}^{\mathrm{B}} = \frac{4}{3}\pi \mathbf{K}_e^{-1} \left(\lambda \mathbf{B}^{\mathrm{II}} + \mathbf{I}\right)^{-1} \mathbf{B}^{\mathrm{I}}, \tag{39}$$

$$\mathbf{R}^{\mathrm{C}} = \frac{4}{3}\pi \left(\kappa \mathbf{C}^{\mathrm{II}} + \mathbf{I}\right)^{-1} \mathbf{C}^{\mathrm{I}} \mathbf{K}_e, \tag{40}$$

where

$$\mathbf{B}^{\mathrm{I}} = \eta\,\omega \mathbf{K}_e^{\frac{1}{2}} \mathbf{A}^{-1} \mathbf{K}_e^{\frac{1}{2}}, \tag{41}$$

$$\mathbf{B}^{\mathrm{II}} = \eta\,\omega \mathbf{K}_e^{\frac{1}{2}} \left(\mathbf{A}^{-1} - \mathbf{I}\right) \mathbf{K}_e^{\frac{1}{2}}, \tag{42}$$

$$\mathbf{C}^{\mathrm{I}} = \eta\,\omega \mathbf{K}_e{}^{-\frac{1}{2}} \left(\mathbf{I} - \mathbf{A}\right)^{-1} \mathbf{K}_e{}^{-\frac{1}{2}}, \tag{43}$$

$$\mathbf{C}^{\mathrm{II}} = \eta\,\omega \mathbf{K}_e{}^{-\frac{1}{2}} \left(\mathbf{A}^{-1} - \mathbf{I}\right)^{-1} \mathbf{K}_e{}^{-\frac{1}{2}}, \tag{44}$$

$$\lambda = \frac{1}{\eta\,\omega K}, \quad \kappa = \frac{K}{\eta\,\omega}. \tag{45}$$

Observe that the expressions (41)-(44) are independent of the intrinsic fracture permeability K. They only depend on $\mathbf{K}_e$ and the geometry of the fractures, through the depolarization tensor $\mathbf{A}$ as defined by (7). Since fractures are modeled as flat ellipsoids, ω is very small, and (41)-(44) can be approximated by their limits as $\omega \to 0$. To evaluate the limits, we need the following relations, which are found from the definition of $\mathbf{A}$ (Eq. (7)) and the fact that $\mathrm{Tr}\mathbf{A} = 1$ (Eq. (9)),

$$\eta\,\omega \mathbf{A}^{-1} = \sum_{i=1}^{2} \frac{1}{\Lambda_i} \tilde{\mathbf{e}}_i \tilde{\mathbf{e}}_i^{\top} + \frac{\eta\,\omega}{1 - \eta\,\omega(\Lambda_1 + \Lambda_2)} \tilde{\mathbf{e}}_3 \tilde{\mathbf{e}}_3^{\top} \tag{46}$$

$$\eta\,\omega \left(\mathbf{A}^{-1} - \mathbf{I}\right) = \sum_{i=1}^{2} \frac{1 - \eta\,\omega\Lambda_i}{\Lambda_i} \tilde{\mathbf{e}}_i \tilde{\mathbf{e}}_i^{\top} + \frac{\eta^2\omega^2\left(\Lambda_1 + \Lambda_2\right)}{1 - \eta\,\omega(\Lambda_1 + \Lambda_2)} \tilde{\mathbf{e}}_3 \tilde{\mathbf{e}}_3^{\top} \tag{47}$$

$$\eta\,\omega \left(\mathbf{I} - \mathbf{A}\right)^{-1} = \sum_{i=1}^{2} \frac{\eta\,\omega}{1 - \eta\,\omega\Lambda_i} \tilde{\mathbf{e}}_i \tilde{\mathbf{e}}_i^{\top} + \frac{1}{\Lambda_1 + \Lambda_2} \tilde{\mathbf{e}}_3 \tilde{\mathbf{e}}_3^{\top} \tag{48}$$

$$\eta\,\omega \left(\mathbf{A}^{-1} - \mathbf{I}\right)^{-1} = \sum_{i=1}^{2} \frac{\eta^2\omega^2\Lambda_i}{1 - \eta\,\omega\Lambda_i} \tilde{\mathbf{e}}_i \tilde{\mathbf{e}}_i^{\top} + \frac{1 - \eta\,\omega\left(\Lambda_1 + \Lambda_2\right)}{\Lambda_1 + \Lambda_2} \tilde{\mathbf{e}}_3 \tilde{\mathbf{e}}_3^{\top}. \tag{49}$$

The vectors $\tilde{\mathbf{e}}_1, \tilde{\mathbf{e}}_2, \tilde{\mathbf{e}}_3$ are given by (6), and Λ_1, Λ_2 are positive scalars given by (8). Taking the limit of Equations (46)-(49), we obtain

$$\lim_{\omega\to 0} \eta\omega \mathbf{A}^{-1} = \lim_{\omega\to 0} \eta\omega \left(\mathbf{A}^{-1} - \mathbf{I}\right) = \sum_{i=1}^{2} \frac{1}{\Lambda_i} \tilde{\mathbf{e}}_i \tilde{\mathbf{e}}_i^{\top}, \tag{50}$$

$$\lim_{\omega\to 0} \eta\omega (\mathbf{I} - \mathbf{A})^{-1} = \lim_{\omega\to 0} \eta\omega \left(\mathbf{A}^{-1} - \mathbf{I}\right)^{-1} = \frac{1}{\Lambda_1 + \Lambda_2} \tilde{\mathbf{e}}_3 \tilde{\mathbf{e}}_3^{\top}. \tag{51}$$

It follows that

$$\lim_{\omega\to 0} \mathbf{B}^{\mathrm{I}} = \lim_{\omega\to 0} \mathbf{B}^{\mathrm{II}} = \mathbf{B} = \mathbf{K}_e^{\frac{1}{2}} \left(\frac{1}{\Lambda_1} \tilde{\mathbf{e}}_1 \tilde{\mathbf{e}}_1^{\top} + \frac{1}{\Lambda_2} \tilde{\mathbf{e}}_2 \tilde{\mathbf{e}}_2^{\top} \right) \mathbf{K}_e^{\frac{1}{2}}, \tag{52}$$

$$\lim_{\omega\to 0} \mathbf{C}^{\mathrm{I}} = \lim_{\omega\to 0} \mathbf{C}^{\mathrm{II}} = \mathbf{C} = \mathbf{K}_e^{-\frac{1}{2}} \left(\frac{1}{\Lambda_1 + \Lambda_2} \tilde{\mathbf{e}}_3 \tilde{\mathbf{e}}_3^{\top} \right) \mathbf{K}_e^{-\frac{1}{2}}. \tag{53}$$

Since we have let $\omega \to 0$, the expressions for Λ_1 and Λ_2 (given by (8)) are reduced to *complete* elliptic integrals, which are efficiently evaluated using a series expansion (Fukushima, 2011b). In the special case where $\eta = 1$ and $\mathbf{K}_e$ is known to be isotropic (for instance, when considering randomly oriented penny-shaped inclusions), we have $\Lambda_1 = \Lambda_2 = \pi/4$, and $\tilde{\mathbf{e}}_1, \tilde{\mathbf{e}}_2, \tilde{\mathbf{e}}_3$ are given by the fracture principal directions $\mathbf{e}_1, \mathbf{e}_2, \mathbf{e}_3$.

We conclude this section by giving the effective medium approximations in the case where all fractures are either open or closed. Recall that, for open fractures, the tensor $\mathbf{R}^{\mathrm{C}}$ do not contribute significantly to the effective permeability. By removing $\mathbf{R}^{\mathrm{C}}$ from (30)-(32), and using the definition of $\mathbf{R}^{\mathrm{B}}$ (Eq. (33)), we have

$$\mathbf{K}_e = \mathbf{K}_0 + \frac{4}{3}\pi \sum_{i=1}^{N} \frac{\varepsilon_i}{\phi_0} \left(\lambda_i \mathbf{B}_i + \mathbf{I}\right)^{-1} \mathbf{B}_i \mathbf{R}_0^{-1}, \quad \text{(Symmetric self-consistent)} \tag{54}$$

$$\mathbf{K}_e = \mathbf{K}_0 + \frac{4}{3}\pi \sum_{i=1}^{N} \varepsilon_i \left(\lambda_i \mathbf{B}_i + \mathbf{I}\right)^{-1} \mathbf{B}_i, \quad \text{(Asymmetric self-consistent)} \tag{55}$$

$$\frac{d\mathbf{K}_e}{d\varepsilon_{sum}} = \frac{4}{3}\pi \sum_{i=1}^{N} \frac{\varepsilon_i}{\varepsilon_{sum}} \left(\lambda_i \mathbf{B}_i + \mathbf{I}\right)^{-1} \mathbf{B}_i, \quad \text{(Differential method)} \tag{56}$$

where $\mathbf{B}_i$ is given by (52). Likewise, if all the fractures are sealed, we can remove $\mathbf{R}^{\mathrm{B}}$ from (36)-(38), and use the definition of $\mathbf{R}^{\mathrm{C}}$ (Eq. (34)) to get

$$\mathbf{K}_e^{-1} = \mathbf{K}_0^{-1} + \frac{4}{3}\pi \sum_{i=1}^{N} \frac{\varepsilon_i}{\phi_0} \left(\kappa_i \mathbf{C}_i + \mathbf{I}\right)^{-1} \mathbf{C}_i \mathbf{K}_e \mathbf{R}_0^{-1} \mathbf{K}_0^{-1}, \quad \text{(Symmetric self-consistent)} \tag{57}$$

$$\mathbf{K}_e^{-1} = \mathbf{K}_0^{-1} + \frac{4}{3}\pi \sum_{i=1}^{N} \varepsilon_i \left(\kappa_i \mathbf{C}_i + \mathbf{I}\right)^{-1} \mathbf{C}_i, \quad \text{(Asymmetric self-consistent)} \tag{58}$$

$$\frac{d\mathbf{K}_e^{-1}}{d\varepsilon_{sum}} = \frac{4}{3}\pi \sum_{i=1}^{N} \frac{\varepsilon_i}{\varepsilon_{sum}} \left(\kappa_i \mathbf{C}_i + \mathbf{I}\right)^{-1} \mathbf{C}_i, \quad \text{(Differential method)} \tag{59}$$

where $\mathbf{C}_i$ is given by (53).

For randomly oriented fractures with $\eta = 1$, the above equations reduce to simple scalar equations. Due to the remark following Eq. (53), the $\mathbf{B}_i$ and $\mathbf{C}_i$ tensors can be found explicitly in this case, and the sum over all fracture orientations becomes a simple uniform average. For open fractures, the resulting expressions are

$$(K_e - K_0)\left(\tfrac{4\lambda}{\pi}K_e + 1\right) = \tfrac{32}{9}\varepsilon\left(\tfrac{2}{3}K_e + \tfrac{1}{3}K_0\right), \quad \text{(Symmetric self-consistent)} \quad (60)$$

$$(K_e - K_0)\left(\tfrac{4\lambda}{\pi}K_e + 1\right) = \tfrac{32}{9}\varepsilon K_e, \quad \text{(Asymmetric self-consistent)} \quad (61)$$

$$\tfrac{4\lambda}{\pi}(K_e - K_0) + \ln(K_e/K_0) = \tfrac{32}{9}\varepsilon, \quad \text{(Differential method)} \quad (62)$$

where we have integrated the differential method using separation of variables. For sealed fractures, the expressions are very similar,

$$\left(K_e^{-1} - K_0^{-1}\right)\left(\tfrac{2\kappa}{\pi}K_e^{-1} + 1\right) = \tfrac{8}{9}\varepsilon\left(\tfrac{2}{3}K_e^{-1} + \tfrac{1}{3}K_0^{-1}\right), \quad \text{(Symmetric self-consistent)} \quad (63)$$

$$\left(K_e^{-1} - K_0^{-1}\right)\left(\tfrac{2\kappa}{\pi}K_e^{-1} + 1\right) = \tfrac{8}{9}\varepsilon K_e^{-1}, \quad \text{(Asymmetric self-consistent)} \quad (64)$$

$$\tfrac{2\kappa}{\pi}\left(K_e^{-1} - K_0^{-1}\right) + \ln(K_0/K_e) = \tfrac{8}{9}\varepsilon. \quad \text{(Differential method)} \quad (65)$$

Eq. (60)-(61) and (63)-(64) are second-degree polynominal equations, which are easily solved analytically. Eq. (62) and (65) are trancendental equations, which can be solved effectively with Newton's method, or with the Lambert W-function (Corless et al, 1996).

Compared with the original effective medium formulas presented in Section (2), Equations (54)-(59) have several advantages. First of all, the original formulations depend on $\mathbf{R}_i$ as defined by (2), which becomes near-singular when ω_i is small and $K_i \gg K_0$ or $K_i \ll K_0$. This limitation is not present in the above expressions, as they are numerically stable regardless of ω_i. Secondly, the new formulations require fewer parameters, since we have substituted ϕ_i, K_i, ω_i with ε_i, λ_i for open fractures and ε_i, κ_i for closed fractures. Finally, Equations (54)-(59) reveal that the effective permeability depends on ω_i and K_i only through their product if fractures are open, and their quotient if the fractures are sealed. This insight is useful if effective medium methods are used in history matching, model calibration or data assimilation problems. Specifically, if K_i and ω_i are regarded as two independent parameters, a parameter estimation algorithm would have problems determining their values, since the effective permeability is only sensitive to their product or quotient. Instead, effective medium methods should be inverted with respect to λ_i for open fractures, and κ_i for sealed fractures.

4 Semi-analytical methods

Apart from effective medium theory, there is also a different approach to fracture permeability upscaling which is widely used. This approach is based on constructing an expression for the upscaled permeability that contains undetermined parameters, and subsequently fit these parameters to numerical simulations. A particularly successful class of these methods is based on the permeability tensor derived by Snow (1969) for infinitely extending open fractures embedded in an impermeable matrix. Oda (1985) extended the Snow model to account for finite-sized fractures, by introducing an empirical connectivity parameter $f \in [0, 1]$ representing the proportion of fractures participating in the connected network. In our notation,

the method of Oda takes the form

$$\mathbf{K}_e = \frac{4}{3}\pi f \sum_{i=1}^{N} \frac{\varepsilon_i}{\lambda_i}\left(\mathbf{I} - \mathbf{n}_i\mathbf{n}_i^{\top}\right), \tag{66}$$

where $\mathbf{n}$ is the normal vector of the fractures.

There have been several attempts to estimate the value of f a priori from statistical fracture parameters (Gueguen and Dienes, 1989; Hestir and Long, 1990; Mourzenko et al, 2004). Recently, Mourzenko et al (2011) presented a very successful model for f as a function of $\rho^{'}$, the mean number of intersections per fracture. The value of $\rho^{'}$ can be calculated a priori for fractures of any convex shape, using the concept of excluded volume (Balberg et al, 1984). In particular, for monodisperse disc-shaped fractures with a finite number of orientations, the mean number of intersections per fracture is given by $\rho^{'} = V_{ex}^{'} \cdot \varepsilon_{sum}$, where

$$V_{ex}^{'} = 4\pi \sum_{i=0}^{n}\sum_{j=0}^{n} \frac{\varepsilon_i}{\varepsilon_{sum}} \frac{\varepsilon_j}{\varepsilon_{sum}} \sin\theta_{ij}, \tag{67}$$

and θ_{ij} is the intersection angle between fracture sets i and j. Thus, $V_{ex}^{'}$ only depends on the orientation distribution of the fractures. When $\rho^{'}$ is smaller than the percolation threshold $\rho_c^{'}$, the fracture network is disconnected and $f = 0$. For $\rho^{'} \geq \rho_c^{'}$, Mourzenko et al (2011) proposed to set $f = g\left(\rho^{'}\right)$, where

$$g\left(\rho^{'}\right) = \frac{\left(\rho^{'} - \rho_c^{'}\right)^2}{\rho^{'}\left(1/\beta + \rho^{'} - \rho_c^{'}\right)}. \tag{68}$$

Both $\rho_c^{'}$ and β are numerically fitted parameters. For $\rho_c^{'}$, we use the proposed value for for disc-shaped fractures, which is $\rho_c^{'} = 2.41$. The value of β for circular fractures is not reported by Mourzenko et al (2011), but it is asserted that β is fairly robust to changes in fracture shape. In this paper, we choose $\beta = 0.180$, which is the value reported for hexagons. An even better match to our numerical results would probably be obtained if the values of β and $\rho_c^{'}$ were fitted to the specific fracture geometries we have studied.

Mourzenko et al (2011) also proposed an extension to (66) for fractures embedded in a permeable matrix. In our notation, the extended model is given by

$$\mathbf{K}_e = \mathbf{K}_0 + h\left(\rho^{'}, \lambda\right) \cdot \frac{4}{3}\pi \sum_{i=1}^{N} \frac{\varepsilon_i}{\lambda_i}\left(\mathbf{I} - \mathbf{n}_i\mathbf{n}_i^{\top}\right), \tag{69}$$

where

$$h\left(\rho^{'}, \lambda\right) = 1 - \frac{1 - g\left(\rho^{'}\right)}{1 + \frac{7}{3}\left(\frac{3}{4}\lambda K_0\right)^{0.7}}, \quad \rho^{'} > 4, \tag{70}$$

and $g\left(\rho^{'}\right)$ is given by (68). When applicable, we will compare the numerical results with the prediction of this model as well.

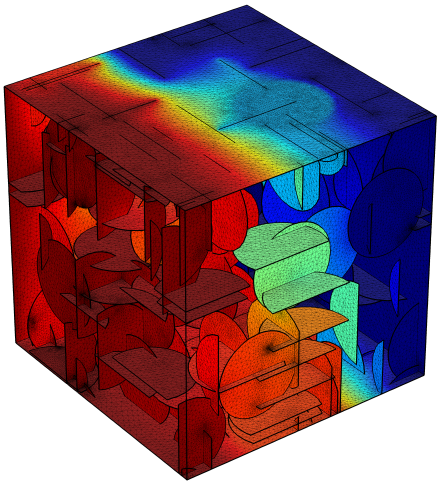

Fig. 3: Sample distribution of fractures from the simulations: Case 5, $\varepsilon_{sum} = 0.4$, second mesh refinement.

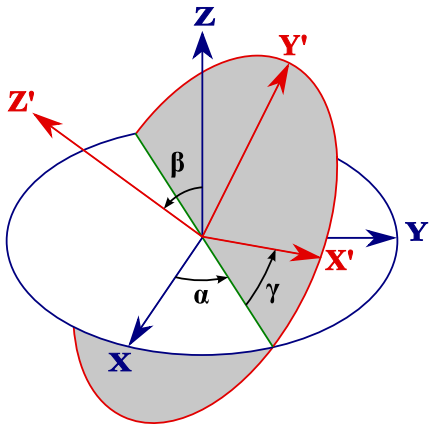

Fig. 4: Euler angles used to describe fracture orientation. Adapted from Brits (2012).

5 Numerical comparisons

In the present computational study, we have selected 10 different test cases (Tab. 2), all corresponding to random, unclustered distributions of equisized, flat ellipsoids. Two of the cases are isotropic, with three orthogonally oriented fracture sets (Case 5 and 6). In the remaining 8 cases, anisotropy is introduced in different ways: Elongated fracture shapes (Cases 1 and 2), fracture sets with unequal densities (Cases 3 and 4) or permeabilities (Cases 7 and 8), and fractures with an oblique intersection angle (Cases 9 and 10). The background permeability was set to be isotropic in all cases. To compute the effective permeability, we generated finite-sized realizations of the fracture geometry, each consisting of 102 fractures within a unit cube.

An example of a typical fracture distribution is shown in Fig. 3. We applied unit pressure difference on two opposing sides, and used a commercial finite-element solver (Comsol Multiphysics®, v. 4.2) to calculate the mean flux, from which the effective permeability was found. This process was repeated for varying fracture radii (up to 1/5 of the cell size) and different matrix/fracture permeability contrasts. Since the result depends on the generated geometry realization, each set of parameters was tested with 20 independent realizations, and the median and interquartile range was computed. Finally, results were compared with analytical predictions.

For the numerical computations, we used flat cylinders (discs) of constant aperture instead of flat ellipsoids, since this is easier to handle numerically. Although thin discs are conceptually different from thin ellipsoids (Pouya and Vu, 2012), our preliminary numerical tests showed that the computed average permeability was not significally affected if thin ellipsoids were substituted with discs of equal radius and volume. Specifically, Case 5 and 6 were computed with both kinds of fracture shapes, for high and low matrix/fracture permeability contrasts. For fracture densities below the percolation threshold, the results were

		α	β	γ	η	$\frac{\kappa}{\kappa_{sum}}$	$\frac{\lambda}{\lambda_{sum}}$	$\frac{\varepsilon}{\varepsilon_{sum}}$	Type
Case 1	Fracture set 1	0°	0°	0°	1/2	-	1	1	Open
Case 2	Fracture set 1	0°	0°	0°	1/2	1	-	1	Sealed
Case 3	Fracture set 1	0°	0°	-	1	-	1/2	2/3	Open
	Fracture set 2	0°	90°	-	1	-	1/2	1/3	Open
Case 4	Fracture set 1	0°	0°	-	1	1/2	-	2/3	Sealed
	Fracture set 2	0°	90°	-	1	1/2	-	1/3	Sealed
Case 5	Fracture set 1	0°	0°	-	1	-	1/3	1/3	Open
	Fracture set 2	0°	90°	-	1	-	1/3	1/3	Open
	Fracture set 3	90°	90°	-	1	-	1/3	1/3	Open
Case 6	Fracture set 1	0°	0°	-	1	1/3	-	1/3	Sealed
	Fracture set 2	0°	90°	-	1	1/3	-	1/3	Sealed
	Fracture set 3	90°	90°	-	1	1/3	-	1/3	Sealed
Case 7	Fracture set 1	0°	0°	-	1	-	1/10	1/3	Open
	Fracture set 2	0°	90°	-	1	-	3/10	1/3	Open
	Fracture set 3	90°	90°	-	1	-	6/10	1/3	Open
Case 8	Fracture set 1	0°	0°	-	1	1/10	-	1/3	Sealed
	Fracture set 2	0°	90°	-	1	3/10	-	1/3	Sealed
	Fracture set 3	90°	90°	-	1	6/10	-	1/3	Sealed
Case 9	Fracture set 1	0°	-22.5°	-	1	-	1/2	1/2	Open
	Fracture set 2	0°	22.5°	-	1	-	1/2	1/2	Open
Case 10	Fracture set 1	0°	-22.5°	-	1	1/2	-	1/2	Sealed
	Fracture set 2	0°	22.5°	-	1	1/2	-	1/2	Sealed

α = dip direction, β = dip angle, γ = rotation, as shown in Fig. 4.
$\kappa_{sum} = \sum \kappa_i$ and $\lambda_{sum} = \sum \lambda_i$, where κ_i and λ_i are given by (45).
$\varepsilon_{sum} = \sum \varepsilon_i$, where ε_i is the fracture density, given by (29).

Tab. 2: The test cases used to assess the performance of the analytical approximations

essentially equal, differing by less than a percent. For large densities, the discrepancy was of the same magnitude as the discretization error, i.e., at most 3%.

Depending on the boundary conditions, calculating the effective permeability of a finite domain amounts to studying a periodic (Fig. 5a) or symmetric (Fig. 5b) array of fractures. None of these configurations are equivalent to an infinite random distribution devoid of long-range correlations, but they are good approximations if there is a large number of fractures within the unit of repetition. Whether periodic or symmetric (isolated) boundary conditions should be used, depends to some degree on the fracture geometry. For instance, if the fracture orientations are not symmetric with the respect to the main axes, symmetric boundary conditions will lead to incorrect results: The equivalent infinite extension is an array of alternating mirror copies of the computational domain, and the mirrored units will have a fracture orientation different from the original ones. On the other hand, if the fracture orientations are indeed mirror symmetric, the effective permeability tensor is known to be diagonal with respect to the main axes. In this case, periodic boundary conditions will give spurious off-diagonal permeability values, while symmetric boundary conditions enforce the correct orientation of the tensor. To obtain more reliable numerical results, we have

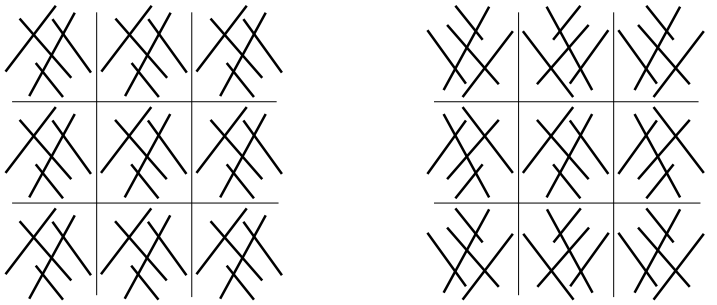

(a) Periodic extension: Periodic boundary conditions

(b) Symmetric extension: Isolated boundary conditions

Fig. 5: Extending a finite domain

chosen to focus on symmetric fracture geometries in this study, with symmetric boundary conditions.

5.1 Mesh considerations

Although conceptually straightforward, numerical experiments are challenging because of the complex geometry of fracture networks. Standard finite-element solvers require the computational mesh to conform with the matrix-fracture interfaces. This is not easy to achieve without compromising standard mesh generation guidelines that ensure well-behaved convergence properties. For instance, if the distribution of fractures is completely random, it may easily happen that two parallel fractures are placed at almost the exact same location, such that the gap between them is much smaller than the fractures themselves. Since the gap must be resolved by the mesh, this leads to either extremely small mesh elements, or elements that are very skewed. The first situation is computationally demanding, the other results in bad numerical properties.

To avoid meshing problems, we created distributions of fractures that were as random as possible while avoiding situations that typically cause the meshing algorithm to fail. Specifically, the realizations were generated by sequentially adding fractures at random locations inside a unit cube. For each addition, we checked whether the edge of the new fracture was barely touching an existing one, in which case the fracture location was slightly changed. The realizations generated by this method were meshable by the software in most cases.

5.2 Numerical errors

In order to use numerical simulations as a benchmark for assessing effective medium approximations, one must be confident that the numerical error can be controlled to a sufficient degree. The main error sources can be divided into two categories:

- Finite-size effects
- Discretization errors

Since the simulations are performed on a finite volume, the calculated permeability depends on the generated realization of the fracture geometry. To get a robust result, each set of parameters was tested with 20 independent realizations, and the sample median and interquartile range (IQR) was computed. The median is a good estimator for the hypothetical "infinite-volume" effective permeability, but it might be biased if the representative volume element (REV) is too small. This is especially true for high-permeable, intersecting fractures close to the percolation threshold, which form fractal patterns that are difficult to resolve within a small volume. To assess the importance of the REV size, we performed a comparison study based on Case 3, 5, 7 and 9. We set the matrix to be impermeable, which allowed us to use 1002 fine-meshed discs per volume since the matrix did not have to be meshed. The computed permeabilities were compared to the original results obtained using 102 discs, and plotted in Fig. 6. Since the matrix permeability is zero, the computed flux scales linearly with the fracture parameter λ, defined by (45). The results are therefore reported using the dimensionless quantity $\mathbf{K}_e \cdot \lambda_1$, where λ_1 refers to the first fracture set in each case, as given in Tab. 2. It is seen that the computed permeability is very robust to changes in the REV size for the cases with three orthogonal fracture sets (Case 5 and 7, Fig. 6b and 6c). In the cases with two sets (Case 3 and 9, Fig. 6a and 6d), it is somewhat more sensitive, especially near the percolation threshold. This dependence is taken into account when the numerical results are interpreted. Ideally, we would like to have used a larger number of discs for the simulations with a permeable matrix as well. But with our current software, it is difficult to increase the number of fractures beyond 100 when the matrix is meshed.

The other potential error source is the discretization error, which is associated with the size and quality of the computational mesh. To estimate this error, each simulation was performed using three different mesh sizes, doubling the number of elements each time. The finest refinement level generated meshes with a typical element size of 0.005 times the domain width. For every refinement, the magnitude of the computed permeability was reduced, which is consistent with the observations of Koudina et al (1998). Our final results were calculated using the finest mesh level, with an applied discretization error correction (typically of magniture 2-3%). The correction was calculated by a Richardson extrapolation scheme, using the results of the coarser meshes (Blum et al, 1986).

The slow numerical convergence, and the difficulties of obtaining a representative finite-sized distribution of fractures, are precisely the reasons why analytical upscaling methods are attractive. For most practical applications, it is infeasible to use as fine meshes and many samples in numerical upscaling routines because of the computational cost. Consequently, a regular coarse-grid numerical upscaling of diffuse fracture networks must be viewed as an approximation with significant inherent uncertainties. In light of this, analytical methods may be an appealing alternative even in situations where their accuracy seems to be moderate.

5.3 Results for open fractures

The general behavior of the analytical methods for open fractures is illustrated by their performance on Case 5, as seen in Fig. 7. This fracture model consists of three fracture families with equal permeability and density, and mutually orthogonal orientations. Thus, the effective permeability of the medium is isotropic.

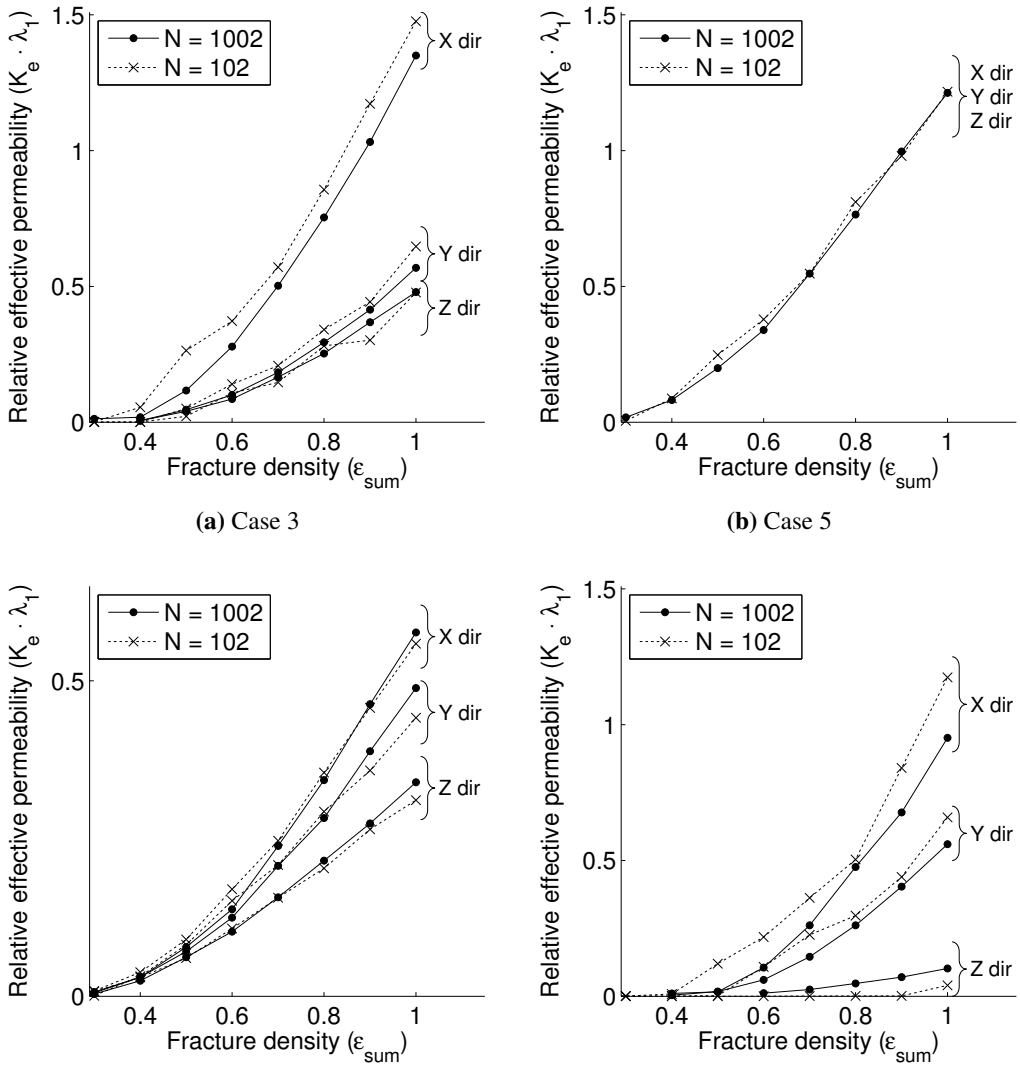

(a) Case 3

(b) Case 5

(c) Case 7

(d) Case 9

Fig. 6: Sensitivity of the REV size

If the contrast between the fracture and matrix permeability is modest (Fig. 7a), the differential method does an excellent job, while the symmetric and asymmetric self-consistent methods slightly underpredicts and overpredicts the permeability, respectively. Since there is significant flow both within the matrix and the fracture network, we see no dramatic change in the effective permeability when the fracture network percolates. The method of Mourzenko et al (2011) also provides a good fit to the numerical data, but it is only applicable for high fracture densities.

For larger matrix-fracture permeability contrasts (Fig. 7b-7c), the differential method gives an increasingly worse estimate of the effective permeability. The self-consistent methods, on the other hand, predict the correct order of magnitude even for large contrasts. In particular, the estimates of the symmetric method agree well with the numerical data. For high fracture densities, the best fit is obtained by the method of Mourzenko et al (2011).

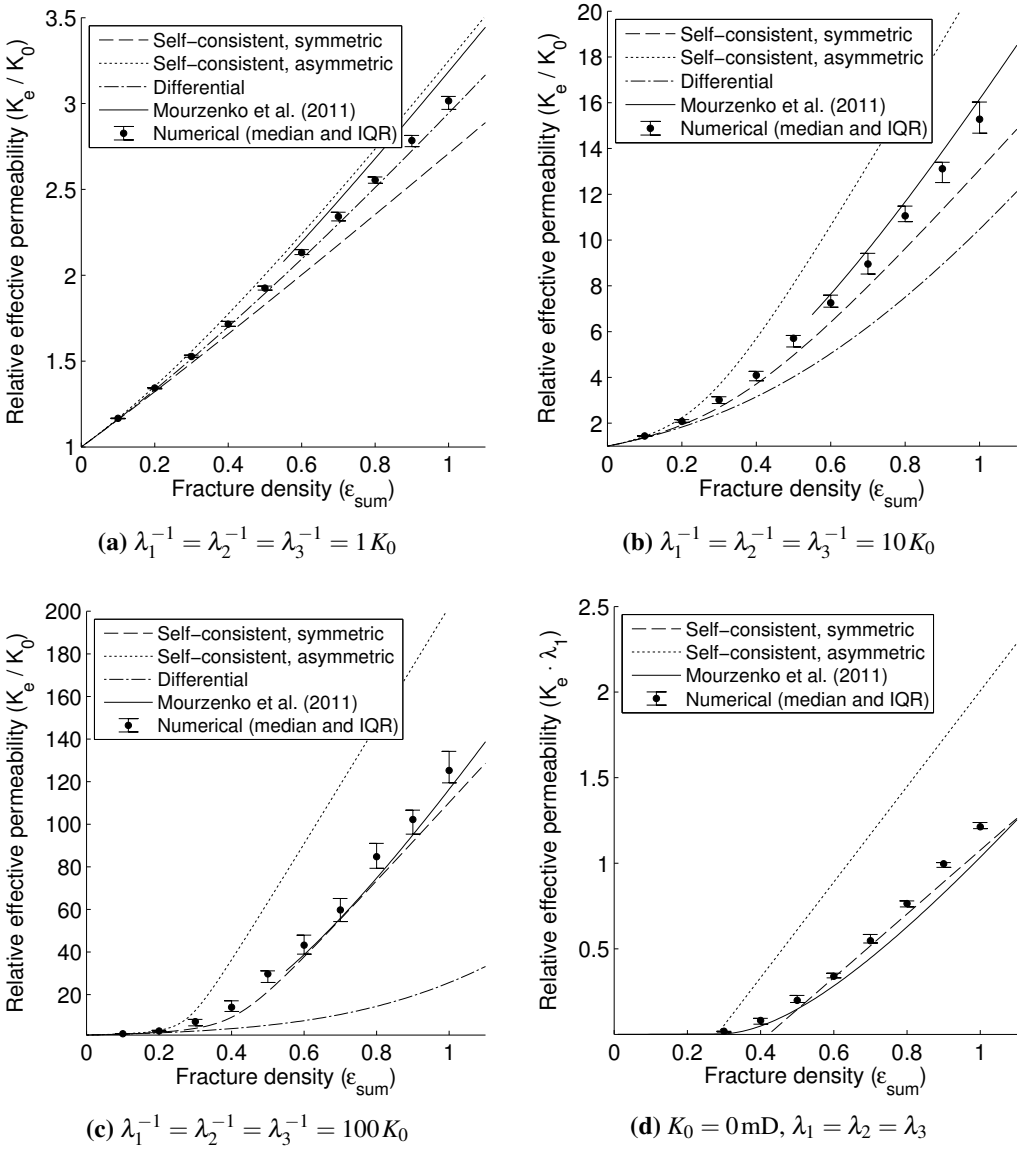

(a) $\lambda_1^{-1} = \lambda_2^{-1} = \lambda_3^{-1} = 1\,K_0$

(b) $\lambda_1^{-1} = \lambda_2^{-1} = \lambda_3^{-1} = 10\,K_0$

(c) $\lambda_1^{-1} = \lambda_2^{-1} = \lambda_3^{-1} = 100\,K_0$

(d) $K_0 = 0\,\mathrm{mD}$, $\lambda_1 = \lambda_2 = \lambda_3$

Fig. 7: Effective permeability, Case 5 (three orthogonal sets, isotropic case)

The most extreme permeability contrast is obtained by setting $\mathbf{K}_0 = 0$ (Fig. 7d). Since the matrix is not meshed in this case, we are able to use 1002 fine-meshed discs per realization, giving very accurate numerical data. As in Fig. 6, results are reported using the dimensionless quantity $\mathbf{K}_e \cdot \lambda_1$, since the permeability scales linearly with the λ parameter when $\mathbf{K}_0 = 0$. Both self-consistent methods are seen to predict a distinct percolation threshold, followed by a linear permeability/fracture density relationship. In fact, the asymmetric method predicts the correct percolation threshold with remarkable accuracy. However, the numerically computed effective permeability increases quadratically past the percolation point, which cause the asymmetric self-consistent approximation to deviate from the numerical. The symmetric self-consistent method is very close to the numerical data even

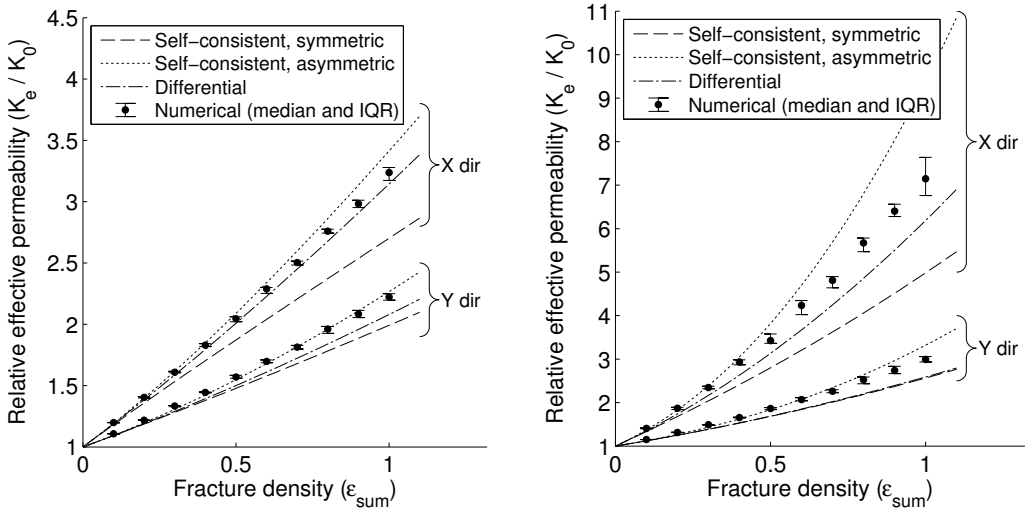

(a) $\lambda_1^{-1} = K_0$ **(b)** $\lambda_1^{-1} = 100\,K_0$

Fig. 8: Effective permeability, Case 1 (single oval fracture set)

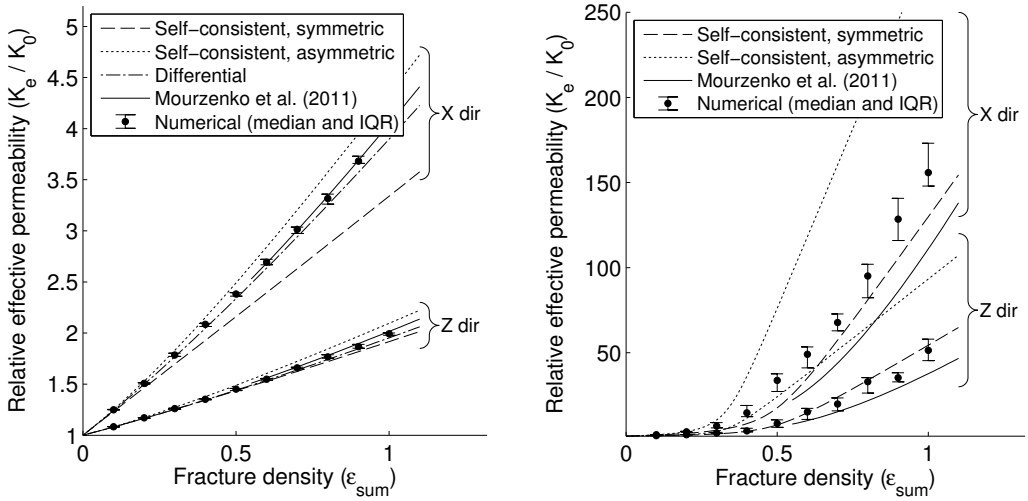

(a) $\lambda_1^{-1} = \lambda_2^{-1} = 1\,K_0$ **(b)** $\lambda_1^{-1} = \lambda_2^{-1} = 100\,K_0$

Fig. 9: Effective permeability, Case 3 (two orthogonal sets, different densities)

though the wrong percolation point is predicted, but the best fit is once again provided by the curve-fitting method.

The performance of the methods is similar in the anisotropic cases, as seen in Fig. 8-11. When interpreting the results, one should also take the REV dependence into account. Fig. 6 shows the REV dependence for Case 3, 5, 7 and 9 when the matrix permeability is zero. Simulations with a permeable matrix are likely to be less sensitive to the REV size, since the impact of each fracture is more local in this case. Thus, Fig. 6 provides a maximal bound on the numerical uncertainty associated with the REV dependence. From the figure, we

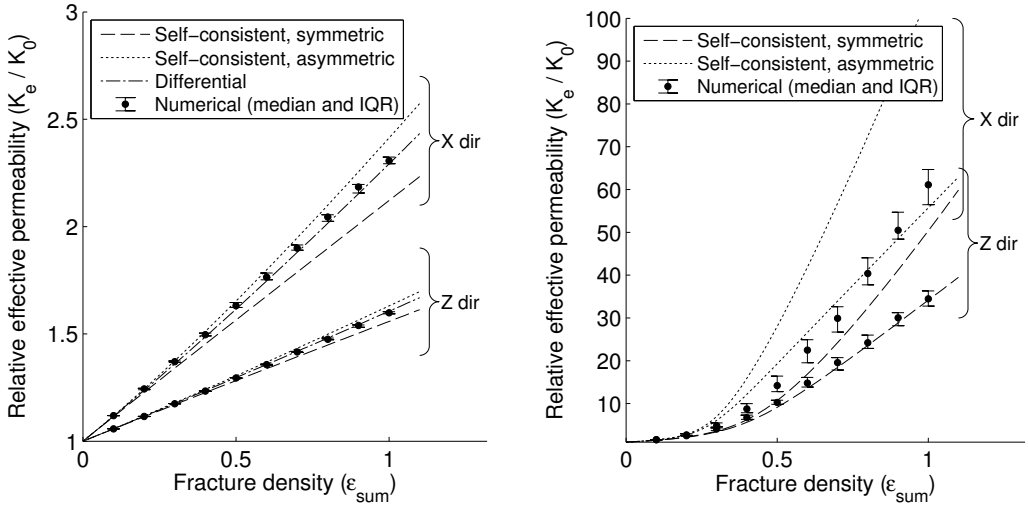

(a) $6\lambda_3^{-1} = 3\lambda_2^{-1} = \lambda_1^{-1} = 1\,K_0$ **(b)** $6\lambda_3^{-1} = 3\lambda_2^{-1} = \lambda_1^{-1} = 100\,K_0$

Fig. 10: Effective permeability, Case 7 (three orthogonal sets, different permeabilities)

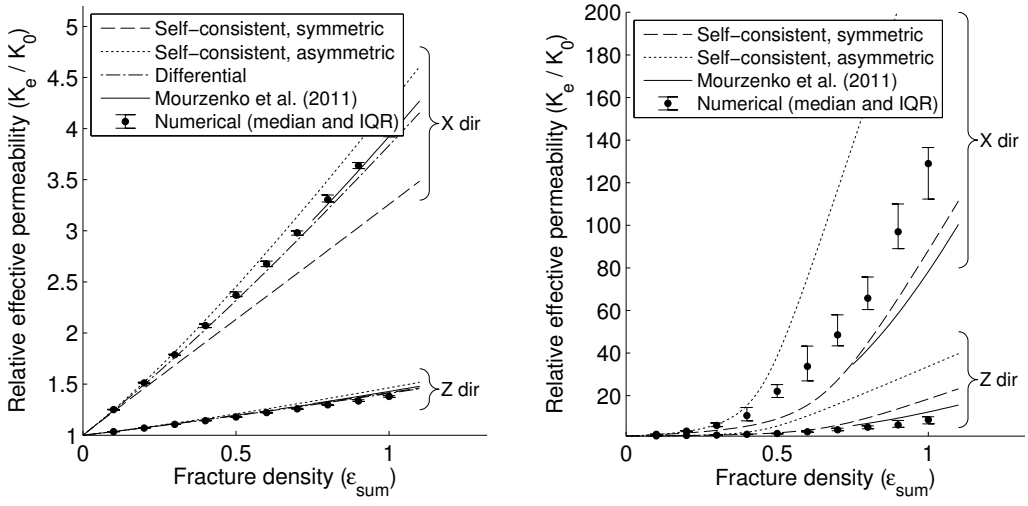

(a) $\lambda_1^{-1} = \lambda_2^{-1} = 1\,K_0$ **(b)** $\lambda_1^{-1} = \lambda_2^{-1} = 100\,K_0$

Fig. 11: Effective permeability, Case 9 (two sets, 45º intersection angle)

can also deduce whether the finite REV size cause the permeability to be underpredicted or overpredicted. For instance, comparing Fig. 6d and Fig. 11b, we can infer that increasing the REV size would probably bring the numerical solution in Fig. 11b closer to the symmetric self-consistent estimate. Unfortunately, our current software is not able to mesh a geometry with more than 100 fractures when both the matrix and fractures must be meshed.

The results in Fig. 8-11 show that the differential approximation is very good when $\lambda^{-1} \approx K_0$ or less. For intersecting fractures with higher permeability contrasts, the differential method quickly becomes useless, and the symmetric self-consistent method seems to

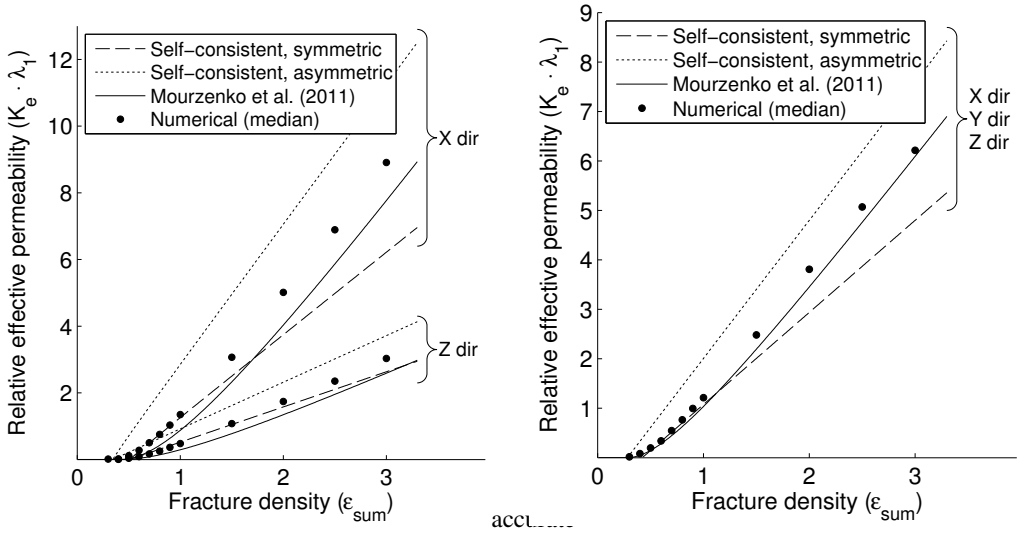

(a) Case 3

(b) Case 5

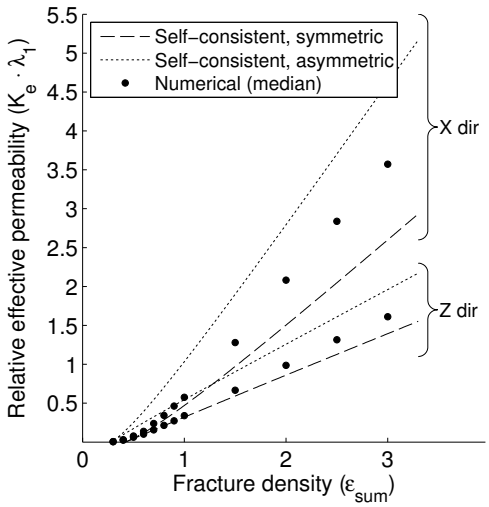

(c) Case 7

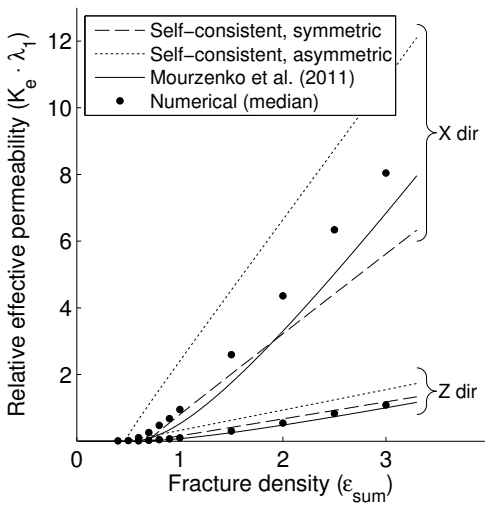

(d) Case 9

Fig. 12: Effective permeability, $K_0 = 0$

be the best choice. Furthermore, the onset of percolation predicted by the asymmetric self-consistent method seems to agree with the numerical data, although the method overpredicts the effective permeability by up to 90 % past the threshold. The method of Mourzenko et al (2011) is not applicable to Case 1 and 7, since Case 1 only contains disconnected fractures, and Case 7 has fractures of different permeabilities. But whenever it can be applied, the method provides a good fit to the data.

To investigate the accuracy of the methods for very high fracture densities and permeability contrasts, we performed a series of numerical simulations with zero matrix permeability and fracture densities up to $\varepsilon_{sum} = 3$. The results are shown in Fig. 12. We used 1002 discs per numerical realization, thus the interquartile range is very small and is omitted from

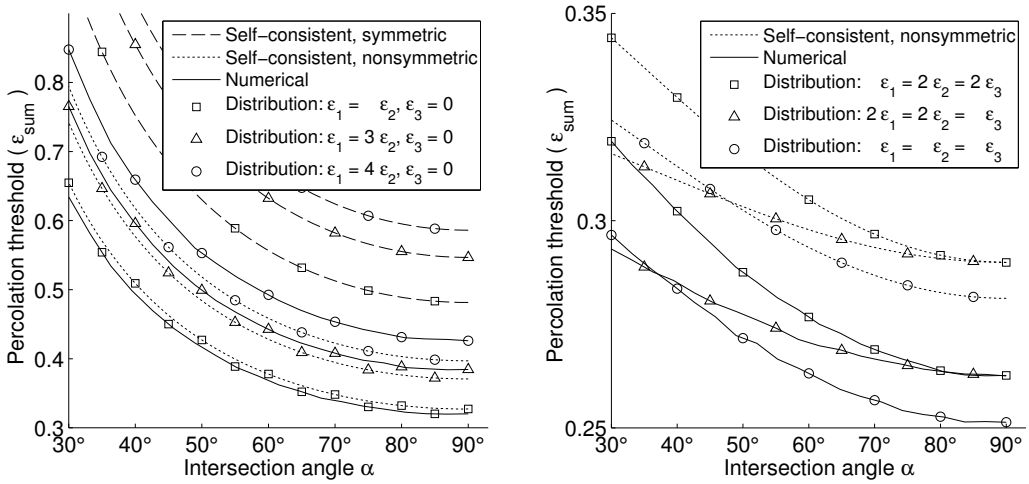

(a) Two intersecting sets **(b)** Three intersecting sets

Fig. 13: Numerical and analytical percolation thresholds

	α	β	γ	η	$\frac{\varepsilon}{\varepsilon_{sum}}$
Fracture set 1	0°	90°	-	1	0.25-0.8
Fracture set 2	30°-90°	90°	-	1	0.2-0.5
Fracture set 3	-	0°	-	1	0-0.5

α = dip direction, β = dip angle, γ = rotation,
as shown in Fig. 4.

Tab. 3: Fracture geometry used for assessing percolation thresholds

the plot. Compared with previous simulations, the symmetric self-consistent approximation is seen to be less accurate for high densities, especially in the anisotropic cases. This might be partially because we have set the matrix shape tensor $\mathbf{H}_0$ to be spherical, despite that the space between the fractures is more elongated at high fracture densities. Our experience with $\mathbf{H}_0$ suggests that other choices for the matrix shape may give more accurate approximations, but we have not been able to find a systematic way of determining the optimal $\mathbf{H}_0$ value. Regarding the asymmetric self-consistent method, Fig. 12 reveals that its estimates are actually better when the fracture density is large. At $\varepsilon_{sum} = 3$, the method overpredicts the permeability by up to 45 %, whereas at $\varepsilon_{sum} = 1$, the overprediction is up to 90 %. Finally, the method of Mourzenko et al (2011) is seen to give a very good fit to the numerical values, and also captures the quadratic increase of permeability with fracture density past the percolation threshold.

The asymmetric self-consistent method is seen to predict percolation thresholds that agree very well with our numerical results, for all the cases we have tested. To further investigate this relationship, we selected an extended number of fracture geometries (see Tab. 3), and calculated the self-consistent percolation thresholds for each of them. These estimates were compared with the true values, obtained using the algorithm of Yi and Tawerghi (2009). The results (Fig. 13) confirm that the symmetric method overpredicts the percolation threshold, while the asymmetric method is surprisingly accurate, especially when there

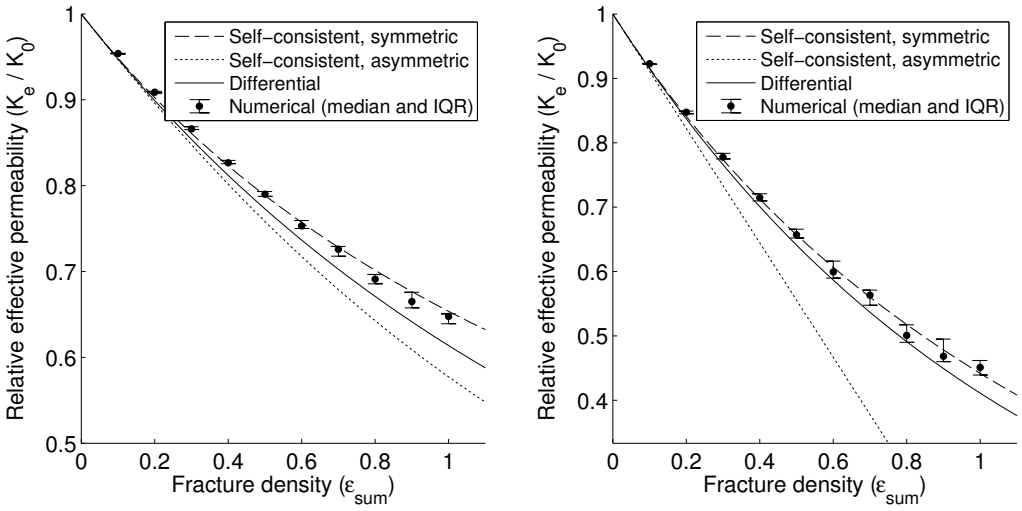

(a) $\kappa_1 = \kappa_2 = \kappa_3 = K_0$ **(b)** $\kappa_1 = \kappa_2 = \kappa_3 = 0.0001\,K_0$

Fig. 14: Effective permeability, Case 6 (three orthogonal sets, isotropic case)

are only two intersecting fracture sets (Fig. 13a). For three sets (Fig. 13b), it overpredicts the threshold slightly, but it is still very close. The threshold's dependence on orientation is captured very well by both self-consistent methods.

Although the fractures were monodisperse in the numerical computation, it was shown by Mourzenko et al (2005) that the size distribution of equishaped fractures has little impact on the percolation threshold, as long as the fracture density is measured by ε_{sum} as defined by (35). Thus, the accuracy of the predicted percolation thresholds, as well as the self-consistent permeability estimates in this section, are likely to be very similar for polydisperse fractures.

5.4 Results for sealed fractures

Finally, we turn to discuss fractures that obstruct the fluid flow. The general behavior of the effective medium methods is illustrated by the isotropic fracture configuration, Case 6, as shown in Fig. 14. The method of Mourzenko et al (2011) is not shown in the plots, since it is only applicable to open fractures. Both the differential and symmetric self-consistent methods perform well on this case, for both modest and large matrix/fracture permeability contrasts. Since fluid flow occurs mainly in the rock matrix, the connectivity of the fracture network (occurring at $\varepsilon_{sum} \approx 0.25$) has no impact on the effective permeability. For very large fracture densities (typically $\varepsilon_{sum} > 5$ (Yi and Esmail, 2012)), the connectivity of the matrix itself is affected, as fractures divide the matrix into disconnected fragments. This happens at a specific fracture density value, called the *void percolation threshold*, where the effective permeability drops to the magnitude of the fracture permeability. The reason of why the asymmetric self-consistent method grossly underpredict the permeability in Fig. 14b, is that it predicts a void percolation threshold at $\varepsilon_{sum} = 1.125$. This is much smaller than the true percolation threshold, which is not visible on the figure.

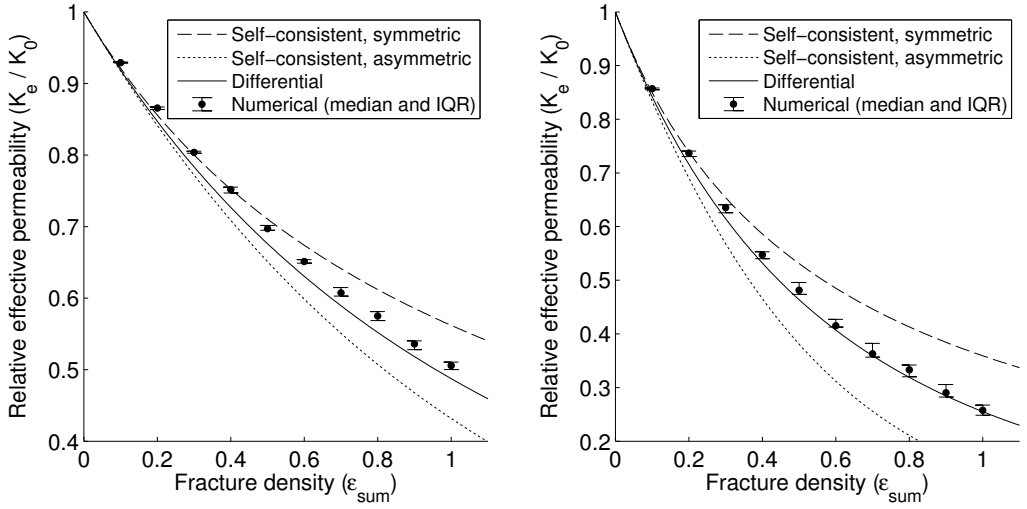

(a) Case 2, Z direction

(b) Case 4, Z direction

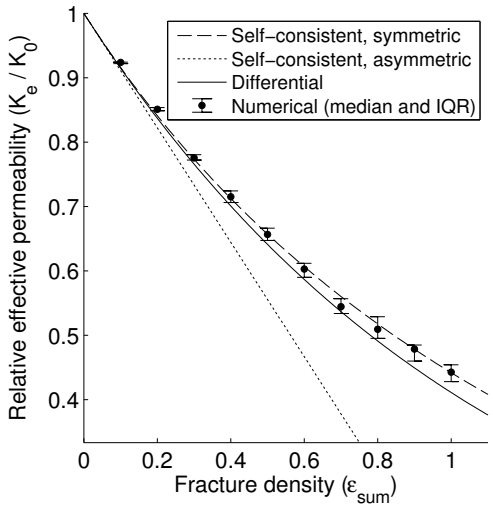

(c) Case 8, X direction

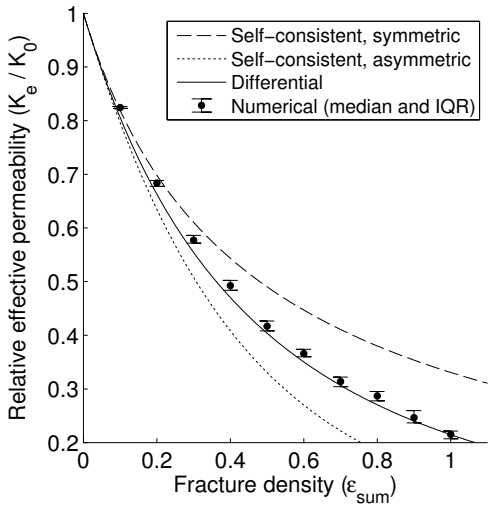

(d) Case 10, Z direction

Fig. 15: Effective permeability, impermeable fractures

In Fig. 15, results for the anisotropic configurations are reported. To reduce the number of plots, only the most significant direction and permeability contrast is shown in each case. The other results are very similar, only that all the analytical approximations are more accurate for smaller permeability contrasts. In general, the differential method is very accurate for all cases that were tested, whereas the asymmetric and symmetric self-consistent methods tend to underpredict and overpredict the permeability, respectively.

6 Summary

In this paper, we have developed a novel set of simplified formulas for three different effective medium methods, in the special case where the matrix inclusions are modeled as flat ellipsoids. Compared to the traditional way of formulating effective medium approximations, the new formulas require fewer input parameters and have improved numerical stability properties.

The accuracy of the methods has been assessed by comparing the analytical predictions with three-dimensional numerical simulations of unclustered random distributions of equisized fractures. A large number of fracture parameters is covered, including different fracture permeabilities, orientations, shapes, intersection angles and number of fracture sets. It is shown that the estimates of the differential method are very accurate for sealed and low-permeable open fractures, at least when the fracture density is less than 1. For high-permeable fractures, the differential method can not be used, unless the fracture density is very low (< 0.1). The semi-analytical method of Mourzenko et al (2011) is usually the most accurate in the high-permeable case, whenever it is applicable.

The self-consistent methods are seen to be applicable to both small and large fracture densities. In particular, the symmetric self-consistent method agrees well with the numerical results for fracture densities less than 1, but is less accurate for larger densities. Only the asymmetric method has the correct asymptotical behaviour for large fracture densities, although it slightly overpredicts the permeability. In general, the asymmetric self-consistent method is seen to consistently overpredict and underpredict the permeability for open and sealed fractures, respectively. The symmetric self-consistent method, on the other hand, mostly underpredicts the permeability of open fractures, and overpredicts the permeability of sealed fractures.

For cases with intersecting, high-permeable fractures, the self-consistent methods predict percolation thresholds at specific fracture densities. Our numerical studies show that the percolation thresholds estimated by the asymmetric self-consistent method are surprisingly accurate, despite the lack of theoretical evidence to support this relationship. It is also very interesting to note that the asymmetric method has the correct physical behaviour for both small and large fracture densities, even though the scheme is not known to be physically realizable.

Acknowledgements The first author acknowledges the support of Statoil ASA through the Akademia agreement.

References

Balberg, I., Alexander, S., Wagner, N. (1984) Excluded volume and its relation to the onset of percolation. Physical Review B 30(7):3933–3943, doi:10.1103/PhysRevB.30.3933

Barthélémy, J.F. (2008) Effective Permeability of Media with a Dense Network of Long and Micro Fractures. Transport in Porous Media 76(1):153–178, doi:10.1007/s11242-008-9241-9

Berryman, J.G., Hoversten, G.M. (2013) Modelling electrical conductivity for earth media with macroscopic fluid-filled fractures. Geophysical Prospecting 61(2):471–493, doi:10.1111/j.1365-2478.2012.01135.x

Blum, H., Lin, Q., Rannacher, R. (1986) Asymptotic error expansion and Richardson extranpolation for linear finite elements. Numerische Mathematik 49(1):11–37, doi:10.1007/BF01389427

Bogdanov, I., Mourzenko, V., Thovert, J.F., Adler, P. (2007) Effective permeability of fractured porous media with power-law distribution of fracture sizes. Physical Review E 76(3):036,309, doi: 10.1103/PhysRevE.76.036309

Brits, L. (2012) Eulerangles.svg. Wikimedia Commons, URL http://en.wikipedia.org/wiki/File:Eulerangles.svg

Bruggeman, D.A.G. (1935) Berechnung verschiedener physikalischer Konstanten von heterogenen Substanzen. I. Dielektrizitätskonstanten und Leitfähigkeiten der Mischkörper aus isotropen Substanzen. Annalen der Physik 416(7):636–664, doi:10.1002/andp.19354160705

Carlson, B.C. (1995) Numerical computation of real or complex elliptic integrals. Numerical Algorithms 10(1):13–26, doi:10.1007/BF02198293

Carlson, B.C., Gustafson, J.L. (1993) Asymptotic approximations for symmetric elliptic integrals. Arxiv preprint math/9310223 9310223

Corless, R.M., Gonnet, G.H., Hare, D.E.G., Jeffrey, D.J., Knuth, D.E. (1996) On the Lambert W function. Advances in Computational Mathematics 5(1):329–359, doi:10.1007/BF02124750

Eshelby, J. (1957) The determination of the elastic field of an ellipsoidal inclusion, and related problems. Proceedings of the Royal Society of 241(1226):376–396

Fokker, P. (2001) General anisotropic effective medium theory for the effective permeability of heterogeneous reservoirs. Transport in porous media 44(2):205–218, doi:10.1023/A:1010770623874

Fossen, H., Schultz, R.A., Shipton, Z.K., Mair, K. (2007) Deformation bands in sandstone: a review. Journal of the Geological Society 164(4):755–769, doi:10.1144/0016-76492006-036

Fukushima, T. (2011a) Precise and fast computation of a general incomplete elliptic integral of second kind by half and double argument transformations. Journal of Computational and Applied Mathematics 235(14):4140–4148, doi:10.1016/j.cam.2011.03.004

Fukushima, T. (2011b) Precise and fast computation of the general complete elliptic integral of the second kind. Mathematics of Computation 80(275):1725–1743

Gueguen, Y., Dienes, J. (1989) Transport properties of rocks from statistics and percolation. Mathematical Geology 21(1):1–13, doi:10.1007/BF00897237

Guéguen, Y., Chelidze, T., Le Ravalec, M. (1997) Microstructures, percolation thresholds, and rock physical properties. Tectonophysics 279(1-4):23–35, doi:10.1016/S0040-1951(97)00132-7

Hestir, K., Long, J.C.S. (1990) Analytical expressions for the permeability of random two-dimensional Poisson fracture networks based on regular lattice percolation and equivalent media theories. Journal of Geophysical Research 95(B13):21,565, doi:10.1029/JB095iB13p21565

Jakobsen, M., Skjervheim, J.A., Aanonsen, S.I. (2007) Characterization of fractured reservoirs by effective medium modelling and joint inversion of seismic and production data. Journal of Seismic Exploration 16:175–197

Koudina, N., Gonzalez Garcia, R., Thovert, J.F., Adler, P. (1998) Permeability of three-dimensional fracture networks. Physical Review E 57(4):4466–4479, doi:10.1103/PhysRevE.57.4466

Landau, L.D., Lifshitz, E.M. (1960) Electrodynamics of continuous media. Pergamon Press

Milton, G.W. (2002) The Theory of Composites. Cambridge University Press, Cambridge, doi: 10.1017/CBO9780511613357, URL http://ebooks.cambridge.org/ref/id/CBO9780511613357

Mourzenko, V., Thovert, J.F., Adler, P. (2004) Macroscopic permeability of three-dimensional fracture networks with power-law size distribution. Physical Review E 69(6):066,307, doi: 10.1103/PhysRevE.69.066307

Mourzenko, V., Thovert, J.F., Adler, P. (2005) Percolation of three-dimensional fracture networks with power-law size distribution. Physical Review E 72(3):036,103, doi:10.1103/PhysRevE.72.036103

Mourzenko, V.V., Thovert, J.F., Adler, P.M. (2011) Permeability of isotropic and anisotropic fracture networks, from the percolation threshold to very large densities. Physical Review E 84(3):036,307, doi: 10.1103/PhysRevE.84.036307

Norris, A., Callegari, A., Sheng, P. (1985) A generalized differential effective medium theory. Journal of the Mechanics and Physics of Solids 33(6):525–543, doi:10.1016/0022-5096(85)90001-8

Oda, M. (1985) Permeability tensor for discontinuous rock masses. Géotechnique 35(4):483–495, doi: 10.1680/geot.1985.35.4.483

Pouya, A., Ghabezloo, S. (2010) Flow Around a Crack in a Porous Matrix and Related Problems. Transport in Porous Media 84(2):511–532, doi:10.1007/s11242-009-9517-8

Pouya, A., Vu, M.N. (2012) Fluid flow and effective permeability of an infinite matrix containing disc-shaped cracks. Advances in Water Resources 42:37–46, doi:10.1016/j.advwatres.2012.03.005

Pozdniakov, S., Tsang, C.F. (2004) A self-consistent approach for calculating the effective hydraulic conductivity of a binary, heterogeneous medium. Water Resources Research 40(5):W05,105, doi: 10.1029/2003WR002617

Singhal, B.B.S., Gupta, R.P. (1999) Applied hydrogeology of fractured rocks. Kluwer Academic Publishers

Snow, D.T. (1969) Anisotropie Permeability of Fractured Media. Water Resources Research 5(6):1273–1289, doi:10.1029/WR005i006p01273

Tawerghi, E., Yi, Y.B. (2009) A computational study on the effective properties of heterogeneous random media containing particulate inclusions. Journal of Physics D: Applied Physics 42(17):175,409, doi: 10.1088/0022-3727/42/17/175409

Torquato, S. (2002) Random Heterogeneous Materials, Interdisciplinary Applied Mathematics, vol 16. Springer New York, New York, NY, doi:10.1007/978-1-4757-6355-3, URL http://link.springer.com/10.1007/978-1-4757-6355-3

Vernerey, F.J. (2012) The Effective Permeability of Cracks and Interfaces in Porous Media. Transport in Porous Media pp 815–829, doi:10.1007/s11242-012-9985-0

Willis, J. (1977) Bounds and self-consistent estimates for the overall properties of anisotropic composites. Journal of the Mechanics and Physics of Solids 25:185–202

Yi, Y., Tawerghi, E. (2009) Geometric percolation thresholds of interpenetrating plates in three-dimensional space. Physical Review E 79(4):1–6, doi:10.1103/PhysRevE.79.041134

Yi, Y.B., Esmail, K. (2012) Computational measurement of void percolation thresholds of oblate particles and thin plate composites. Journal of Applied Physics 111(12):124,903, doi:10.1063/1.4730333

Zimmerman, R.W., Yeo, I. (2000) Fluid Flow in Rock Fractures: From the Navier-Stokes Equations to the Cubic Law. In: Faybishenko, B., Witherspoon, P.A., Benson, S.M. (eds) Dynamics of fluids in fractured rock, American Geophysical Union